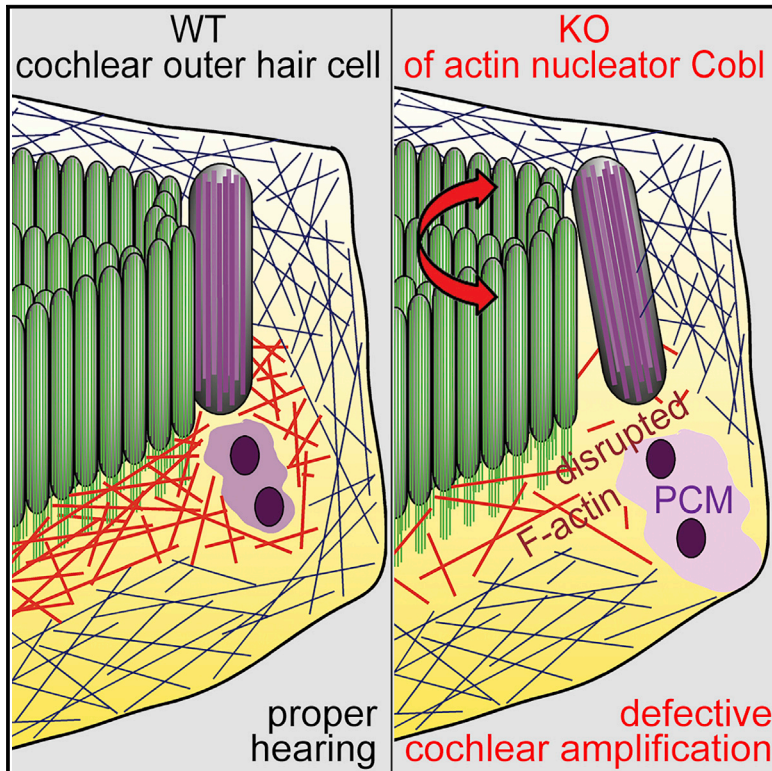# The Actin Nucleator Cobl Is Critical for Centriolar Positioning, Postnatal Planar Cell Polarity Refinement, and Function of the Cochlea

Graphical Abstract

Authors

Natja Haag, Susann Schüler, Sandor Nietzsche, Christian A. Hübner, Nicola Strenzke, Britta Qualmann, Michael M. Kessels

Correspondence

britta.qualmann@med.uni-jena.de (B.Q.), michael.kessels@med.uni-jena.de (M.M.K.)

In Brief

Haag et al. identify the actin nucleator Cobl as a crucial effector of postnatal planar cell polarity refinements and for cochlear amplification during hearing. The authors show that F-actin-dependent PCM organization, centriolar positioning, kinocilium regression, PCM/kinociliar alignment with stereocilia, and sensory apparatus orientation are cellular mechanisms derailed upon *Cobl* KO.

Highlights

- Cobl is critical for cochlear amplification in hearing

- Cobl is a critical effector of postnatal planar cell polarity refinement

- Cobl KO led to reduction of cuticular plate F-actin beneath the sensory apparatus

- Cobl KO disrupts F-actin-dependent PCM organization and the PCM-stereocilia alignment

The Actin Nucleator Cobl Is Critical for Centriolar Positioning, Postnatal Planar Cell Polarity Refinement, and Function of the Cochlea

Natja Haag,[1,5] Susann Schüler,[1] Sandor Nietzsche,[2] Christian A. Hübner,[3] Nicola Strenzke,[4] Britta Qualmann,[1,*] and Michael M. Kessels[1,6,*]

[1]Institute of Biochemistry I, Jena University Hospital - Friedrich Schiller University Jena, 07743 Jena, Germany
[2]EM Center, Jena University Hospital - Friedrich Schiller University Jena, 07743 Jena, Germany
[3]Institute of Human Genetics, Jena University Hospital - Friedrich Schiller University Jena, 07743 Jena, Germany
[4]InnerEarLab, Department of Otolaryngology, University of Göttingen, 37075 Göttingen, Germany
[5]Present address: Institute of Human Genetics, University Hospital RWTH Aachen, Aachen, Germany
[6]Lead Contact
*Correspondence: britta.qualmann@med.uni-jena.de (B.Q.), michael.kessels@med.uni-jena.de (M.M.K.)
 https://doi.org/10.1016/j.celrep.2018.07.087

SUMMARY

Proper cochlear hair cell array development and sensory apparatus positioning are achieved by planar cell polarity signaling. Effectors executing proper tissue development and maturation programs are largely unknown. We show that the actin nucleator Cobl is an important effector in postnatal refinement and maintenance of planar cell polarity. During the critical time of hearing onset, these polarity defects coincided with reduced F-actin beneath the sensory apparatus and with premature kinocilium retraction. These defects were accompanied by organizational defects of the pericentriolar scaffold that coincided with basal body and centriolar mispositionings. Importantly, the pericentriolar defects observed in *Cobl* KO mice were demonstrated to be actin polymerization dependent and calcium/calmodulin signaling dependent. Because *Cobl* KO phenotypes manifested postnatally, planar cell polarity is not solely an important developmental process. The Cobl-dependent planar cell polarity maintenance and refinement processes we describe here seem critical for hearing, as *Cobl* KO mice show deficient cochlear amplification.

INTRODUCTION

Establishment and changes of cell morphology and polarity depend on forces created by actin and microtubule cytoskeletal structures. Early embryonic planar cell polarity (PCP) plays a central role in tissue patterning (Montcouquiol et al., 2003; Curtin et al., 2003). PCP signaling, for example, brings about a preliminary alignment of outer hair cells (OHCs) in the inner ear and of their stereocilia bundles serving as mechanosensors. Auditory perception in mice starts about

2 weeks after birth (Song et al., 2006). Sound-evoked basilar membrane vibrations cause stereociliar deflections and open mechanotransduction channels (Fettiplace and Hackney, 2006).

While microtubule-based ciliary structures are indicative of PCP and also the orientation of OHC stereociliar bundles in the cochlea precisely reflects PCP in the tissue (Kelley et al., 2009; Ezan and Montcouquiol, 2013), little is known about PCP effectors and about postnatal processes subsequent to classical embryonic PCP signaling.

Stereocilia of OHCs are organized as V-shaped bundles inserted into the cortical actin network, the cuticular plate (Tilney et al., 1980; Kitajiri et al., 2010; Szarama et al., 2012). They show tight correlation with the microtubule-based kinocilium intimately associated with the tip of the stereocilia bundle. The kinocilium originates from a mother centriole-derived basal body and may play some guiding role in PCP and stereocilia positioning, as it migrates to the distal (i.e., abneural) hair cell side during embryonic development. Recent work in simplified systems suggested some, albeit not yet fully understood F-actin cross talk with centrosomes and centrioles (Farina et al., 2016; Carvajal-Gonzalez et al., 2016; Obino et al., 2016).

Here, we demonstrate at the whole-animal level that Cobl (Cordon-Bleu) (Ahuja et al., 2007)—a WH2 domain-based actin nucleator (Qualmann and Kessels, 2009)—is critical for cross talk of microtubule-based and F-actin-based structures in OHCs of the cochlea. *Cobl* knockout (KO) hereby specifically impaired F-actin structures and functions in the cuticular plate beneath stereocilia and the kinocilium. *Cobl* KO disrupted the organization of the pericentriolar material (PCM) and its intimate spatial alignments with the kinocilium and the stereocilia bundle. Interestingly, the associated stereociliar positioning defects mostly manifested postnatally, that is, were not related to classical embryonic PCP signaling. *Cobl* KO phenotypes thereby unveiled postnatal refinements and also revealed that PCP has to be actively maintained during adulthood. Physiological studies uncovered that Cobl-mediated functions in the cochlea are important for the OHC amplifier function in hearing.
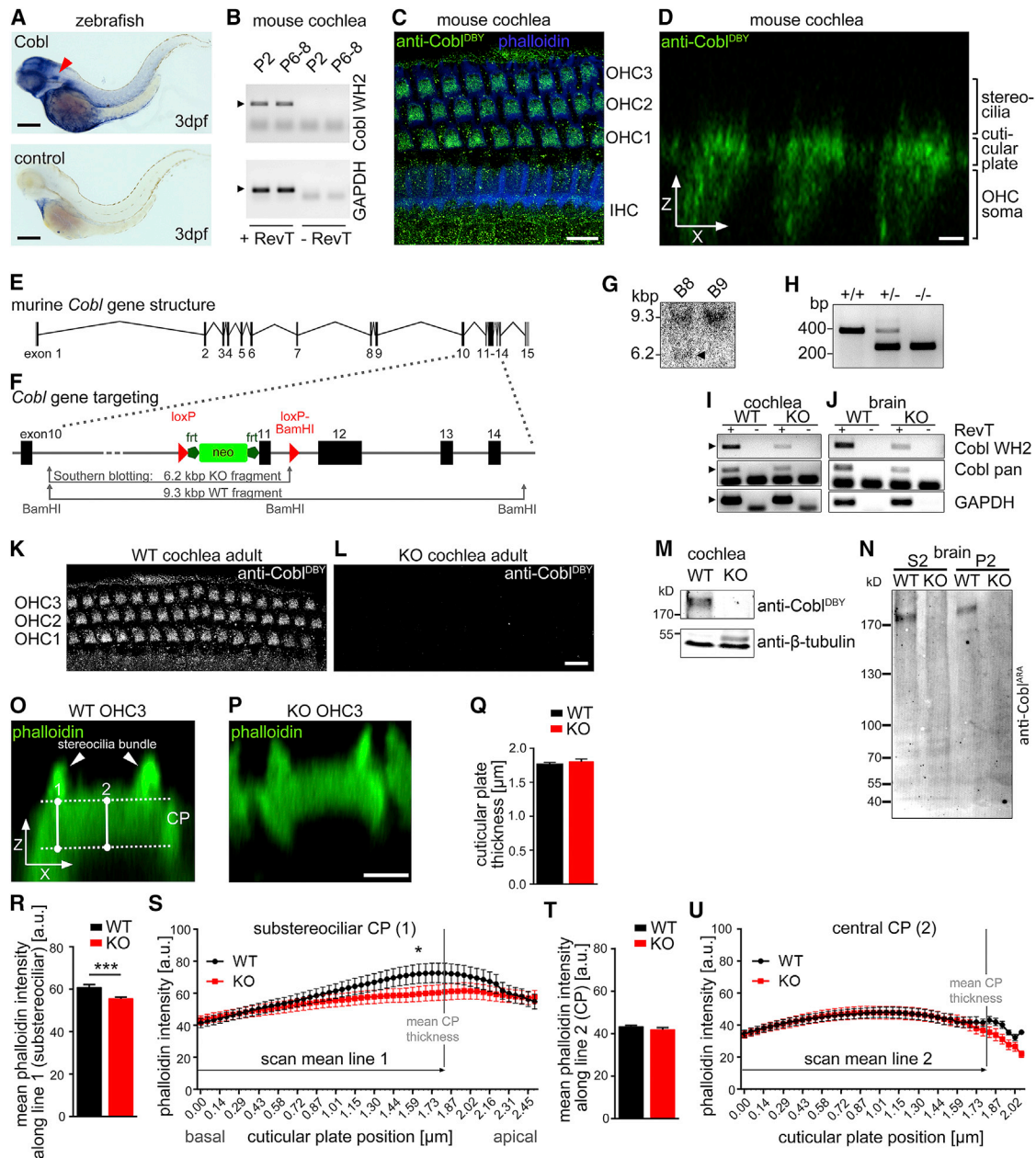
Figure 1. *Cobl* KO Mice Show a Lack of a Specific Cortical F-Actin Subset Residing beneath the Sensory Apparatus of OHCs in the Inner Ear

(A) Whole-mount *in situ* hybridization (3 days post-fertilization [dpf] zebrafish). Arrowhead, Cobl expression in the ear. Control, sense probe. Bar, 200 μm.

(B) Cobl RT-PCR analyses in P2 and P6–P8 murine cochleae. Controls, GAPDH and without reverse transcriptase (−RevT).

(C) Maximum intensity projection (MIP) of anti-Cobl immunosignals (green) and phalloidin (blue) in cochlear hair cells of adult mice. Bar, 10 μm.

(D) Orthogonal view (z/x-plane) of OHC3 cells shown in (C). Bar, 2 μm.

(E) The murine *Cobl* gene (dark gray, coding exons).

(F) Targeting vector (Cre/lox). Neo, neomycin resistance.

(G) Southern blot of two ES cell clones (B8 and B9). Shown are wild-type (9.3 kbp; B8 and B9) and transgenic (6.2 kbp; B8; arrowhead) genomic DNA fragments (BamHI restriction; see F).

(H) Genotyping of pups from heterozygous breedings.

(I and J) RT-PCR analysis shows a strong *Cobl* mRNA decay in general (pan) and of all WH2 domain-containing *Cobl* isoforms in cochleae (I) and brains (J) of *Cobl* KO mice.

(K and L) Anti-Cobl^DBY immunosignals in OHCs from WT (K) versus *Cobl* KO cochleae (L). Bar, 10 μm. WT image, overview (C) is taken from.

(M) Anti-Cobl^DBY immunoblotting of cochlear extracts showing the absence of the actin nucleator Cobl upon *Cobl* KO.

(legend continued on next page)

RESULTS

Cobl KO Mice Show a Lack of a Specific Cortical Subset of Actin Filaments

Cobl promotes F-actin formation and is critical for dendrite formation and branching in neurons (Ahuja et al., 2007; Hou et al., 2015, 2018). *In situ* hybridizations of zebrafish larvae suggested an additional role in the auditory system. Strong *Cobl* signals also occurred in the developing ear (Figure 1A). In mice, cochlear Cobl expression was detected, too (Figure 1B). Cobl was prominent in OHCs and enriched in their cuticular plates (Figures 1C and 1D).

To analyze its functional importance, we generated *Cobl* KO mice. The murine *Cobl* gene comprises 15 exons (GenBank: NM_172496.3). Database analyses predict that besides the actin nucleator Cobl also a splice variant lacking exons 10-15, that is, all WH2 domains, may exist (CoblΔE10-15). Antibodies against the N-terminal part of Cobl (anti-Cobl[ARA]; Schwintzer et al., 2011), which would detect both Cobl and the putative truncated variant not representing an actin nucleator, did not yield any immunosignals in samples from up to ten pooled cochleae due to the minimal tissue amounts (not shown). Therefore, these analyses could not exclude that a CoblΔE10-15 protein may exist. RT-PCRs could also not rule out that indeed some actin nucleation-incompetent ΔE10-15 variant may exist, as some weak mRNA trace was obtained with E9 and I9 primers (Figures S1A–S1C).

To eradicate specifically all actin nucleating products of the *Cobl* gene but not the putative truncated form, which lacks all actin-binding WH2 domains and thus would have functions unrelated to actin nucleation, we targeted exon 11 (Cre/lox). Using mice ubiquitously expressing Cre (Schwenk et al., 1995), we removed exon 11 together with the selection cassette yielding a mouse line with an ubiquitous and constitutive *Cobl* KO (Figures 1E–1N).

RT-PCRs demonstrated that exon 11 deletion affected Cobl mRNA stability in cochlea and brain (Figures 1I and 1J). Western blotting as well as immunofluorescence analyses of cochleae and brain material with antibodies against a C-terminal epitope (Figure S1A; Haag et al., 2012) confirmed that the actin nucleator Cobl was successfully knocked out (Figures 1K–1N).

Theoretically, a residual fragment of 549 aa (544 + 5 non-Cobl amino acids due to frameshift; $\sim$60 kDa) could result from exon 11 deletion (Figure S1B). Whereas antibodies against Cobl[175-324] (anti-Cobl[ARA]) did successfully detect Cobl in brains of wild-type (WT) mice, neither the putative ΔE10-15 variant nor any truncated protein resulting from exon 11 deletion was detected in KO samples (Figure 1N).

Homozygous *Cobl* KO mice displayed normal viability during >1 year of monitoring. Body weights of both sexes were unaltered. Litter sizes were significantly reduced when homozygous mice were bred. These impairments, however, did not seem to reflect a critical role of Cobl during embryonic development, as suggested by work in zebrafish (Ravanelli and Klingensmith, 2011; Schüler et al., 2013), because genotypes did not differ from Mendelian distribution (Figures S1D–S1G).

Cobl KO embryos did not display any obvious defects in embryogenesis, in body laterality establishment (data not shown), or in neural tube closure, and did also not lead to exencephaly, which would have been an obvious readout for defects in cerebrospinal fluid movements through the ventricular system (Figures S1H and S1I). Thus, although Cobl is expressed in the floor plate and in the notochord of the neural tube at embryonic day 9.5 (E9.5) (Figures S1J–S1M), as demonstrated before at the mRNA level (Gasca et al., 1995; Carroll et al., 2003), *Cobl* KO mice did not show any phenotypes reflecting impairments of motile cilia or defects in early development based on the parameters examined.

To address a putative Cobl role in the cochlea, we first examined the F-actin-rich cuticular plates of OHCs (Figures 1O–1U). Their width increases during cochlear maturation (Szarama et al., 2012). This was not affected upon *Cobl* KO (Figures 1O–1Q). However, specifically areas beneath the sensory apparatus showed a significantly reduced F-actin content in *Cobl* KO OHCs (Figures 1R–1U). The overall reduction across the entire line scan was about 10% (Figure 1R). Interestingly, distribution analyses showed that the F-actin loss occurred specifically in an about 1-μm-thick apical layer underneath OHC stereocilia. In this substereociliar layer, the F-actin loss reached $\sim$20% (Figure 1S).

Altered Organization of PCM in *Cobl* KO Cochleae

The cell cortex embeds both stereocilia and kinocilium base structures. Three-dimensional (3D) surface models computed from postnatal day 8 (P8) cochleae immunostained for pericentrin, a marker for the PCM surrounding the centrioles at the kinocilium base (Doxsey et al., 1994), showed a dramatically increased volume of the pericentriolar scaffold. In all three OHC rows, it more than doubled (Figures 2A–2E). The sum intensity of the anti-pericentrin labeling was also increased (Figure 2F). This may reflect an increased pericentrin recruitment in *Cobl* KO mice, an improved immunodetection upon a loss of PCM compression, or both. Since the density of the anti-pericentrin labeling in the enlarged PCM was decreased (Figure 2G), PCM organization clearly was impaired. Similar defects—albeit not yet as pronounced—were seen in newborn mice (P2) (Figures S2A–S2G).

In contrast to the defects in PCM organization, the centrioles encased by the PCM (marked by immunolabeling of γ-tubulin; Jones et al., 2008) did not show any significant defects (Figures S2H and S2I). *Cobl* KO thus specifically disrupted the organization of the pericentrin-marked PCM around centrioles.

(N) Anti-Cobl[ARA] antibodies detect Cobl but no putative truncated protein or ΔE10-15 variant (see Figures S1A–S1C) in brain.

(O–U) Blinded F-actin analyses in WT (O) and *Cobl* KO cochlear whole-mount preparations (P8) (P) using line scans across the cuticular plate at substereociliar (line 1) and stereocilia-free positions (line 2). Dashed lines, cuticular plate borders (O). Bar, 2 μm.
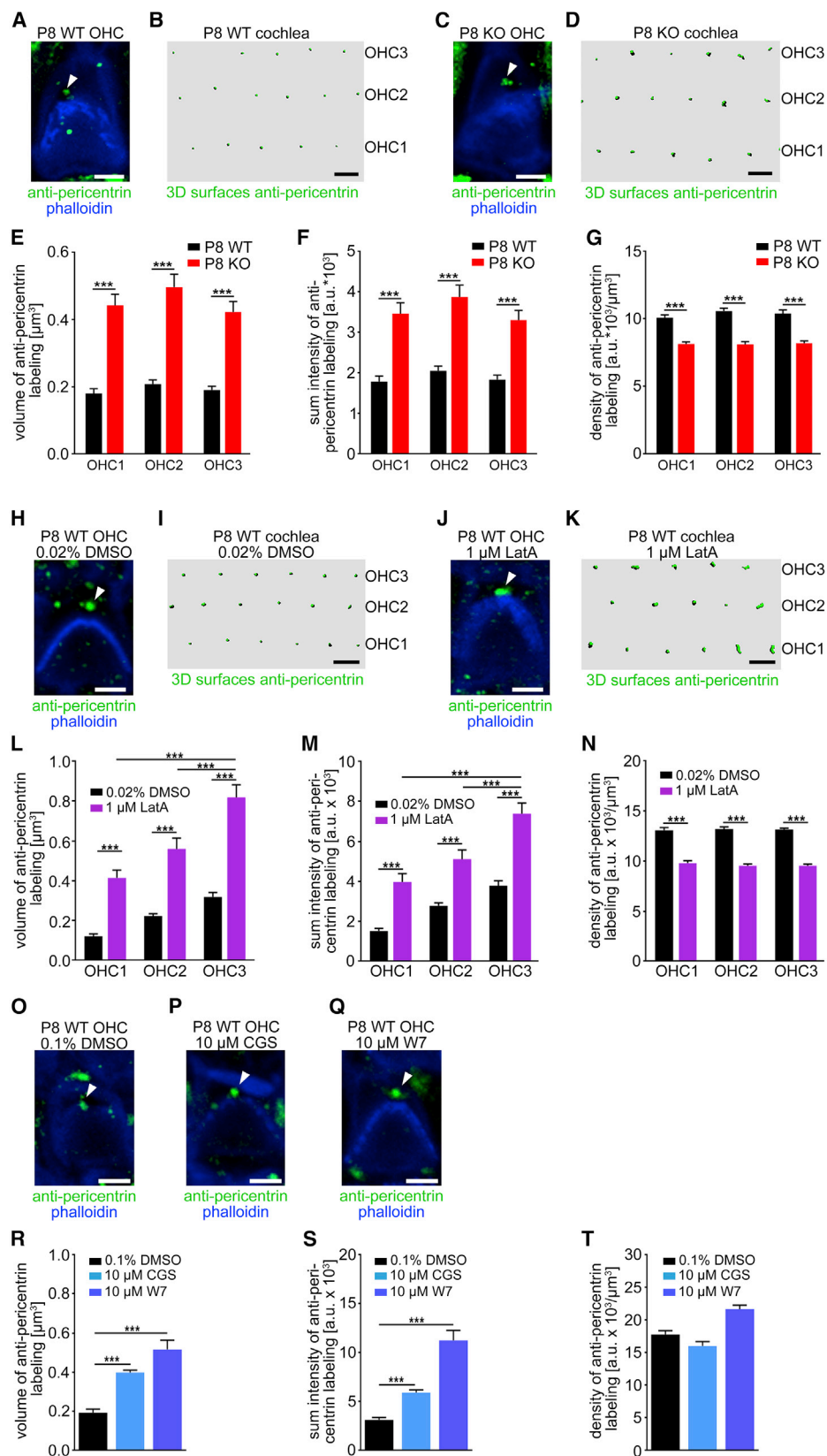
(Q) OHC3 cuticular plate thicknesses.

(R–U) Mean phalloidin intensities (R and T) and distribution of phalloidin intensities (S and U) in line 1 (R and S) and in line 2 scans (T and U) of n = WT/KO 33/33 OHC3s; 3/4 animals. Data, mean and SEM.

(R) ***p < 0.001 (unpaired, two-tailed t test).

(S) *p < 0.05 (two-way ANOVA/Sidak's test).

See also Figure S1.

(legend on next page)

Proper PCM Organization in OHCs Depends on Actin Filament Formation and Ca²⁺/CaM Signaling

To address whether the PCM organization defects observed upon KO of the actin nucleator Cobl reflect a critical role of F-actin formation, we applied 1 μM latrunculin A to freshly dissected cochlear whole mounts of P8 WT animals. Strikingly, this resulted in an increase in PCM volume and sum anti-pericentrin signal (Figures 2H–2M) as well as in a decrease of anti-pericentrin immunolabeling density (Figure 2N). Thus, suppression of F-actin formation by latrunculin A mirrored the defects observed in *Cobl* KO mice very well (Figures 2A–2G versus Figures 2H–2N).

Cobl's actin functions in neurons depend on Ca²⁺/CaM signaling (Hou et al., 2015). Strikingly, CaM inhibitors CGS9343B and W7 both also led to a dramatic loss of PCM organization reminiscent of the *Cobl* KO phenotypes. The PCM volume more than doubled and the sum anti-pericentrin signal increased strongly (Figures 2O–2T).

Together, these experiments demonstrate that Cobl and proper F-actin formation play key roles in organizing the PCM surrounding the centrioles, that is, the kinociliar base, and that this cell biological process is dependent on Ca²⁺/CaM signaling.

The Defects in PCM Organization Coincide with Impaired Centriole Positioning

Proper positioning of centrioles is considered key in the development of organized cellular arrays. Three consequences of PCM disorganization for the OHC sensory array seemed plausible: First, since the PCM harbors the two centrioles, their positioning to each other could be affected. Second, impairments of the PCM at the base of the kinocilium may affect kinocilium organization and stability. Third, consequences for the stereocilia bundle that is linked to the kinocilium during development seemed possible—especially, if the tight alignment of the mother centriole (basal body) and/or of the PCM with the tip position of the stereocilia bundle would be disrupted.

First, *Cobl* KO indeed coincided with impaired centriole positioning. 3D analyses of immunolabelings of γ-tubulin showed that the intercentriolar distance was increased in P2 *Cobl* KO OHCs (Figures 3A–3C and S3A).

Cobl KO Impairs PCM-Kinocilium Alignment and Causes Premature Kinocilium Retraction prior to Hearing Onset

Second, we addressed whether the PCM disorganization would coincide with impairments in kinocilium linkage and subsequently with defects in kinocilium stability. Strikingly, 3D reconstructions of OHCs of P2 cochlea stained for pericentrin and for acetylated tubulin (axoneme marker; Figures S3B and S3C) showed that basal body docking to the axoneme of the kinocilium was affected upon *Cobl* KO. Specifically in the more mature OHC1 and OHC2 cells, the PCM-to-kinocilium base distance was increased by about 25% (Figures 3D–3I).

The fate of kinocilia was examined next. *Cobl* KO animals showed a premature kinocilium retraction. While at P2 and P6 invariably every OHC still had a kinocilium and at P15 the kinocilium had disappeared from almost all WT and *Cobl* KO OHCs, we observed significantly fewer kinocilia-bearing OHC3s in *Cobl* KO cochleae during the critical time window of cochlear maturation prior to hearing onset (P8) (Figures 3J–3T). At P9, premature kinocilium retraction was even more severe. Now, all three OHCs rows of the apico-medial turn of *Cobl* KO cochleae showed significantly fewer remaining kinocilia (Figures 3P, 3Q, and 3T).

Cobl KO Leads to Disrupted Spatial Correlation of the Kinocilium with the Stereocilia Bundle

We then addressed the third possibility and explored whether the Cobl- and actin filament formation-dependent defects in PCM organization may disrupt the normally tight kinocilium/stereocilia bundle alignment. As the kinocilium showed premature regression at P8 and P9 in *Cobl* KO mice and both PCM as well as centriole positioning defects were already observable in newborn *Cobl* KO mice (Figures 2 and 3), we addressed this question in newborn mice. Strikingly, scanning electron microscopy (EM) revealed that the tight spatial correlation of the kinociliar base and the stereocilia bundle was disrupted upon *Cobl* KO (Figures 4A and 4B). Analyses of images with the same rotational positioning of the cochlear array (Figures 4C and 4D) showed that the distance of the kinociliar base to the stereocilia bundle was significantly increased. In *Cobl* KO OHC3s, the distance increased by almost 30% (to >420 nm) when compared to WT—a significant disruption of the normally very intimate assembly of the kinocilium with the tip of the stereocilia bundle (Figure 4E).

3D analyses of surface-rendered anti-pericentrin immunostained PCMs and of phalloidin-highlighted stereocilia bundles demonstrated that also the PCM and the base of the stereocilia bundle tip were misaligned in all three OHC rows (Figures 4F–4J).

Interestingly and in accordance with the relatively symmetrical positioning of the kinocilia at the tip of the V-shaped stereocilia bundles (Figures 4A–4D), we did not observe any shift of the


Figure 2. *Cobl* KO Causes an Impaired Kinociliar Base Organization that Is Phenocopied by Inhibition of F-Actin Formation and Ca²⁺/CaM Signaling in WT Cochlea

(A–D) MIPs of whole-mount preparations (A and C) and corresponding 3D surface renderings (B and D) of P8 WT (A and B) and *Cobl* KO (C and D) cochleae (green, pericentrin; blue, phalloidin).

(E–G) Analyses of PCMs for volume (E), sum intensity (F), and density (sum intensity/volume) (G) of anti-pericentrin labeling. n = WT/KO 692/769 OHCs, 20/22 images, 5 animals each.

(H–T) Corresponding analyses with cochleae of P8 WT mice incubated with DMSO (control) (H, I, L–N, O, and R–T), latrunculin A (LatA) (J–N), and with the CaM inhibitors CGS9343B (CGS) (P and R–T) and W7 (Q–T).

Bars, 1 μm (A, C, H, J, and O–Q) and 5 μm (B, D, I, and K). (L–N and R–T) Quantitative analyses of anti-pericentrin signals. n = 44–269 OHCs and 3–4 WT P8 cochleae/condition. Data, mean + SEM. ***p < 0.001. Two-way ANOVA/Tukey's (E–G and L–N) and one-way ANOVA/Dunnett's (R–T). White arrowheads (A, C, H, J, and O–Q) mark PCMs (confirmed by associated kinociliar anti-acetylated tubulin labeling; not shown). See also Figure S2.
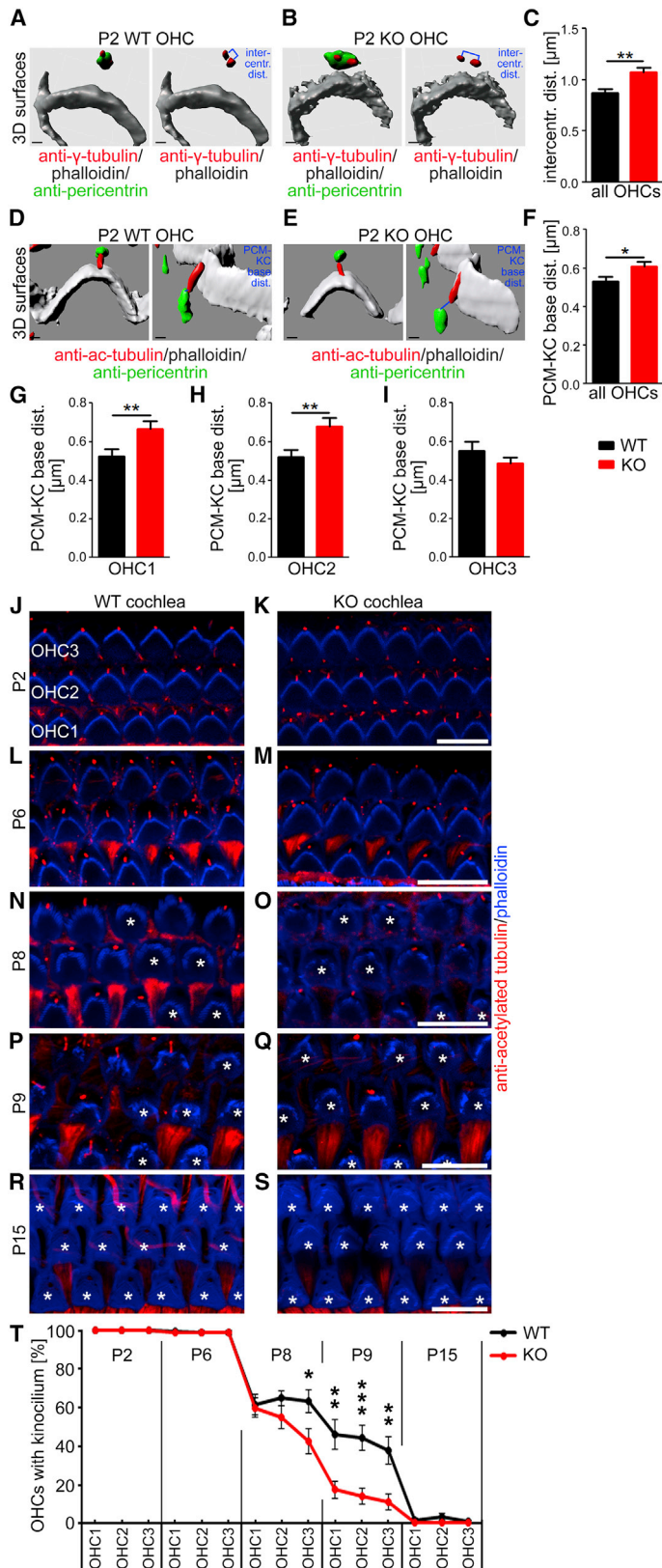
Figure 3. *Cobl* KO Leads to Increased Intercentriolar Distance, Disrupted PCM-to-Kinocilium Base Alignment, and Premature Kinocilium Regression prior to Hearing Onset

(A–C) Analyses of intercentriolar distances in 3D reconstructions of anti-γ-tubulin labelings (centriolar marker) costained for PCMs (anti-pericentrin) and stereocilia bundles (phalloidin) in P2 *Cobl* KO OHCs compared to WT (A and B).

(C) Quantitative analyses of n = WT/KO 61/97 OHCs; 3/3 cochleae and mice.

(D–I) Analyses of PCM-to-kinocilium (PCM-KC) base distances in 3D surface renderings of anti-acetylated tubulin (marker for the axoneme of kinocilia), anti-pericentrin and phalloidin-stained P2 cochleae of WT (D) and *Cobl* KO mice (E). Panels in (D) and (E) show both a top view (left) and a corresponding side view (right). Bars, 0.5 μm (A–D). (F–I) Quantitations of OHCs overall (n = WT/KO 175/219 OHCs; 4/4 mice) (F) and row for row (G–I) (n = 56–75 each row).

(J–S) MIPs of confocal z stacks of P2 (J and K), P6 (L and M), P8 (N and O), P9 (P and Q), and P15 (R and S) WT (J, L, N, P, and R) and *Cobl* KO cochleae (K, M, O, Q, and S) stained with anti-acetylated tubulin antibodies (red; kinocilia) and phalloidin (blue; stereocilia bundles). White asterisks, hair cells without kinocilium. Bars, 10 μm.

(T) Quantitation of kinocilium-bearing WT and *Cobl* KO OHCs at P2, P6, P8, P9, and P15 (120–769 OHCs; 8–33 images; 2–6 animals/each stage and genotype).

Data, mean and SEM. Unpaired two-tailed t test. *p < 0.05; **p < 0.01; ***p < 0.001. See also Figure S3.
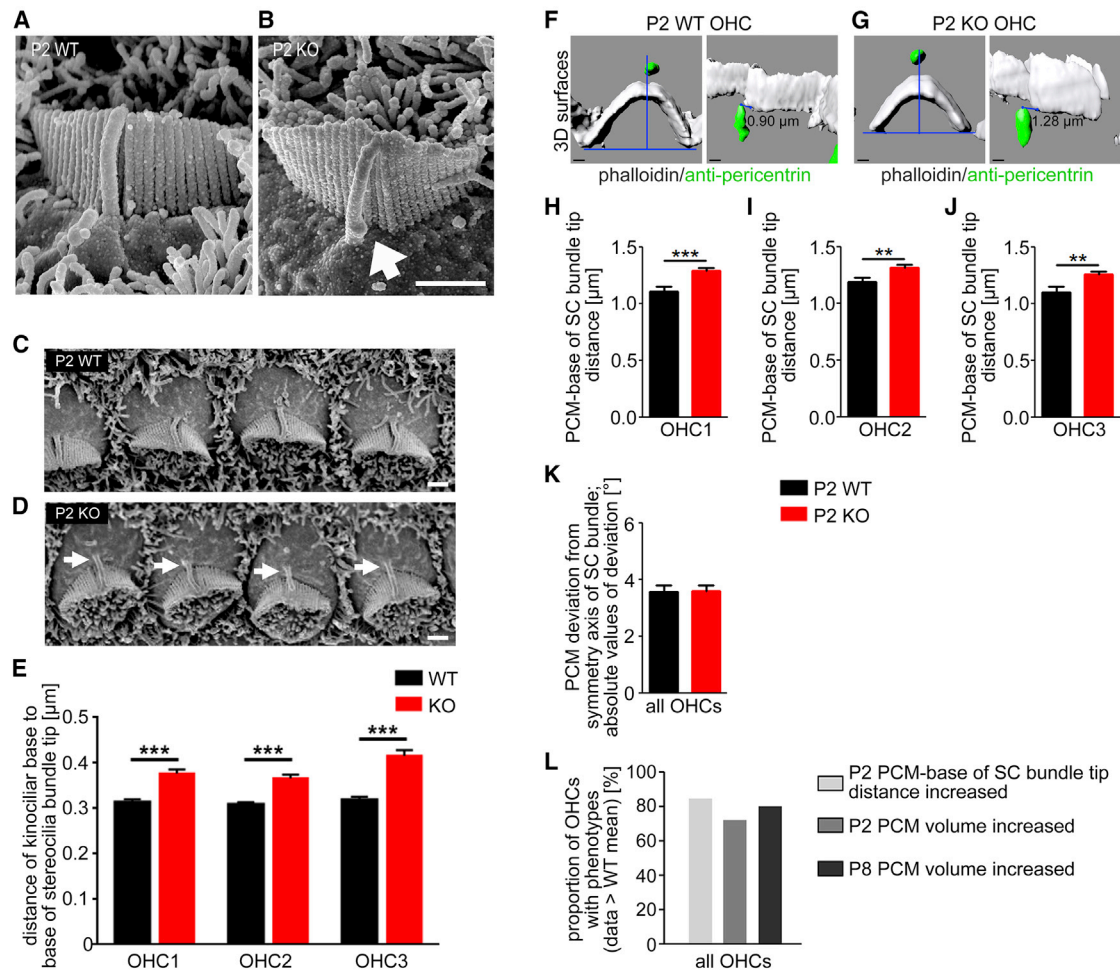
Figure 4. *Cobl* KO Leads to a Disruption of the Spatial Correlation between the Kinocilium and the Stereocilia Bundle

(A–D) High-resolution scanning EM images showing a disrupted correlation of the kinocilium with the stereocilia bundle in *Cobl* KO OHC3s (A and B) and example of top views of cochlear arrays in similar overall specimen orientation used to quantitatively evaluate the spatial correlations between kinocilia and stereocilia bundles (C and D). Arrows marks the significantly widened gap between kinociliar base and stereocilia bundles. Bars, 1 μm.

(E) Distances of kinociliar base to first stereocilium of one side of the bundle. n = 60 OHCs/row and genotype (4 cochleae and animals each). Data, mean + SEM; two-way ANOVA/Bonferroni's.

(F and G) Anti-pericentrin and phalloidin-stained P2 cochleae of WT (F) and *Cobl* KO mice (G) analyzed for PCM-to-stereocilium docking (left 3D surface renderings show orientation for lateral deviation determination; right panels visualize examples of increased distance of PCM and stereocilia bundle).

(H–J) Distances between PCM (apical point) to the base of the stereocilia bundle tip in OHC1 (H), OHC2 (I), and OHC3 (J) (n = WT/KO 171/224 OHCs; 49–75 OHCs/row).

(K) Deviation of PCM positions from the stereocilia bundles symmetry axis (perpendicular blue line in left panels of F and G) (n = WT/KO 221/234 OHCs) (both 4/4 animals). Data, mean + SEM. Unpaired, two-tailed t test.

(L) Comparison of the proportions of OHCs with indicated phenotypes (percentage of cells above WT mean).

$**p < 0.01$; $***p < 0.001$. See also Figure S4.

PCM to one side of the stereocilia bundle (Figure 4K), as described for defects in classical embryonic PCP signaling (Gegg et al., 2014). Instead, the disruption of the alignment of the PCM (i.e., the kinocilia base) with the stereocilia bundle occurred along the symmetry axis.

The fact that the proportion of OHCs that showed a disorganized PCM as well as structural defects in kinocilia docking to the stereocilia bundle tip was about 80% suggests that these *Cobl* KO phenotypes do not occur separately from each other but may be correlated (Figure 4L).

Cobl KO Leads to Rotational Defects in OHC Arrays of Adult *Cobl* KO Cochleae that Reflect Impairments of Postnatal PCP Refinements and Maintenance

Considering that proper ciliary functions and a tight coupling of kinocilia to stereocilia are thought to be linked to PCP signaling and/or establishment in some way (Frolenkov et al., 2004; Kelley et al., 2009; Ezan and Montcouquiol, 2013), the *Cobl* KO phenotypes identified thus far could have consequences for stereocilia bundle positioning. Scanning EM analyses indeed showed that the sensory arrays of OHCs were
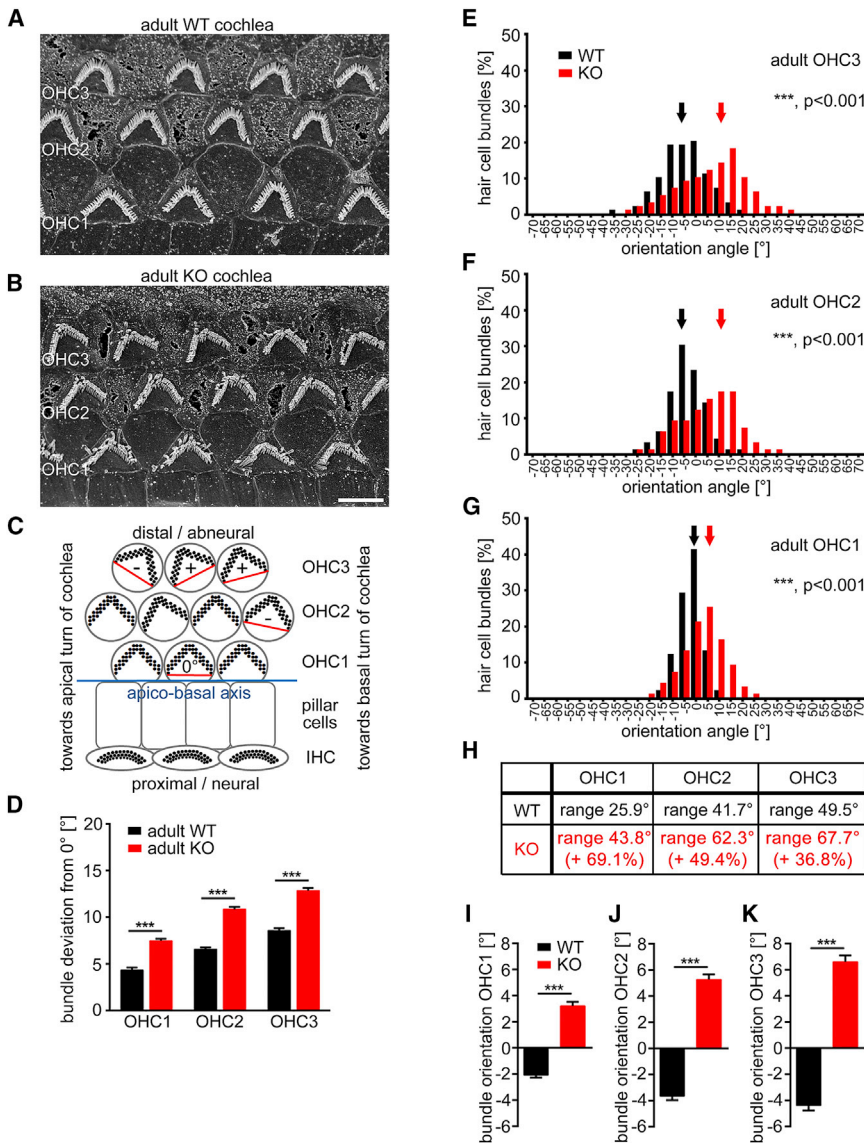
Figure 5. Defective Planar OHC Polarity and Directed Rotational Shift of Stereocilia Bundles in Adult *Cobl* KO OHCs

(A and B) Scanning EM of stereocilia bundles of adult (12–15 weeks) WT (A) and *Cobl* KO cochlea (B) for orientation evaluations. Bar, 2 μm.

(C) Scheme depicting the determinations. 0°, horizontal position, that is, alignment to apico-basal axis (blue line); rotations, +, turned toward apical turn; −, turned toward basal turn of the cochlea.

(D) The absolute values of stereocilia bundle deviations from 0° (irrespective of direction of misalignment).

(E–G) Distributions of stereocilia bundle orientations (classes shown represent the 5° around indicated values) in OHC3 (E), OHC2 (F), and OHC1 (G) of adult WT and *Cobl* KO cochleae. Arrows, middle of three highest groups for each genotype.

(H) Ranges of stereocilia bundle orientation angles (red, extended ranges).
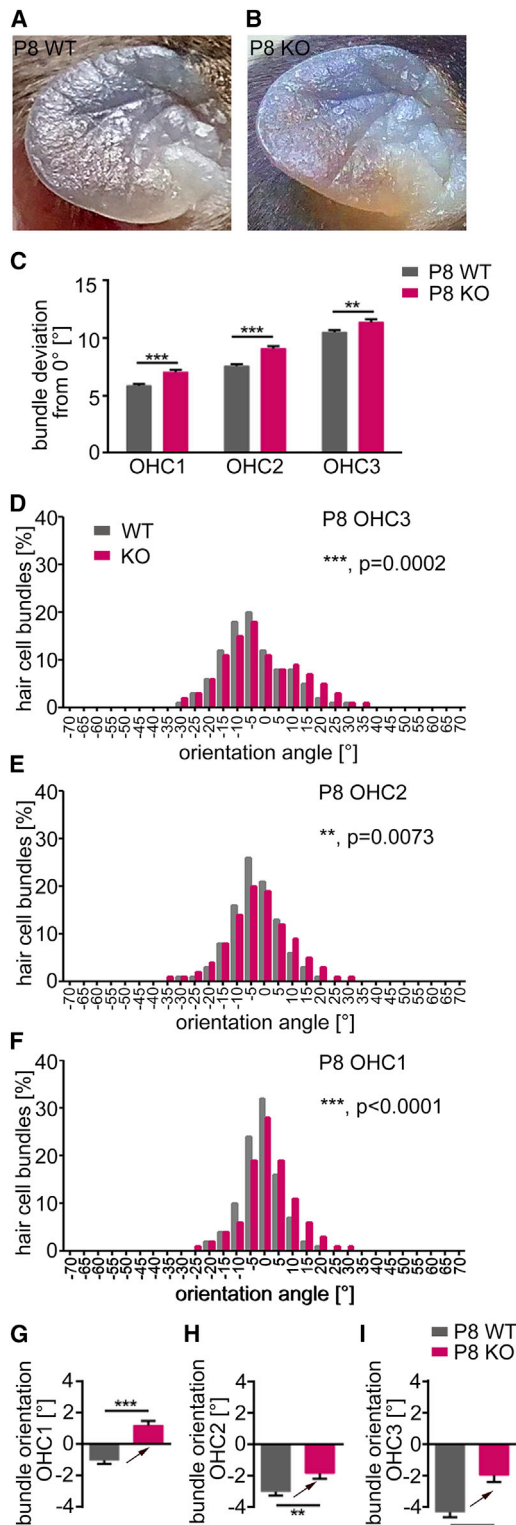
(I–K) Averaged orientation angles of OHC1 (I), OHC2 (J), and OHC3 (K). Note the orientation of *Cobl* KO OHC stereocilia bundles toward the apical turn of the cochlea, that is, opposite to WT. n = 705–874 hair cell bundles/row; 17–53 images/cochlea; 4 animals and cochleae/genotype.

Data, mean and SEM. ***p < 0.001; two-way ANOVA/Bonferroni's (D) and D'Agostino normality/Mann-Whitney U (E–G and I–K). See also Figure S5.

increased, as shown by measuring the total range of angle distributions. In absolute numbers, the ranges of deviations from the corresponding means were 18–20°, that is, 37%–69% larger than in WT (Figures 5H and S5).

Second, in contrast to the often erratically directed deviations found upon disrupting embryonic PCP signaling (e.g., Copley et al., 2013; Ezan et al., 2013), the orientation deficits in *Cobl* KO mice showed directionality of the deviations. *Cobl* KO OHCs showed a general rotational distortion of stereocilia bundles toward the apical turn of the cochlea (+). This rotation was in clear contrast to WT, which rather displayed rotations toward the basal turn (−) (Figures 5I–5K).

Kinocilia and/or basal body disruptions in, for example, *Kif3a*, *Bbs8*, and *Ift20* KO coincided with impairments in cochlear development and were linked to grossly misoriented stereocilia bundles indicative of disrupted embryonic PCP signaling (Sipe and Lu, 2011; May-Simera et al., 2015). It was therefore of utmost importance to clarify whether the stereociliar orientation defects seen in young adult *Cobl* KO mice represent defects in classical embryonic PCP. Interestingly, this was not the case. Scanning EM demonstrated that OHC stereocilia bundles in newborn (P2) *Cobl* KO pups were correctly located, orientated, and aligned after the completion of embryonic development (Figures S6A–S6I).

altered upon *Cobl* KO (Figure 5). Whereas neither individual stereocilia in the bundles nor the bundles themselves showed any obvious defects (erect, normal three-row staircase pattern, normal height gradation, all three rows with normal extent and undisturbed packing and no distortions in the row linearity or any gaps; Figure S4), we observed a broader range of orientation angles of OHC stereocilia bundles in cochlea of young adult *Cobl* KO mice (Figures 5A and 5B). Quantitation of orientation angles of stereocilia bundles according to literature procedures (absolute deviations from 0°) (e.g., Dabdoub et al., 2003; Copley et al., 2013; Ezan et al., 2013) showed a less regular alignment in *Cobl* KO cochleae when compared to WT. The orientation deviations reached 13° (OHC3) and were 40%–70% above WT and highly statistically significant in all three OHC rows (Figure 5D). Interestingly, *Cobl* KO hereby led to a superimposition of two effects (Figures 5E–5G and S5). First, the ranges of orientations of OHC stereocilia were

Figure 6. *Cobl* KO Leads to Defects in Postnatal Directed Rotational Refinement

(A and B) Heads of WT (A) and *Cobl* KO pups (B) with ears still closed at P8.

(C–I) Quantitative scanning EM analyses of OHC stereocilia bundle orientations directly prior to hearing onset (P8).

Only row 3 OHCs showed a widened range of distributions, which may reflect the fact that OHC maturation follows a gradient from OHC1 to OHC3 (Frolenkov et al., 2004) (Figures S6F–S6I). However, in average, the OHCs of all three rows were orientated around 0° in both *Cobl* KO and WT newborns (Figures S6J–S6L). This average orientation is in line with a report describing a minor, postnatal minus-directed rotation of specifically OHC3 stereocilia bundles between P0 and P4 with OHC3s being orientated close to 0° at P4 (Copley et al., 2013).

Consistent with undisturbed classical embryonic PCP signaling and successful distinction between distal and proximal sides, also the PCP markers Par6b and aPKC (Ezan and Montcouquiol, 2013) were properly localized to the proximal side in both WT and *Cobl* KO OHCs (Figures S6M and S6N).

Taken together, classical embryonic PCP signaling seems not to be affected by *Cobl* KO. This provided an excellent opportunity to unveil postnatal processes important for stereocilia bundle orientation. Our examinations clearly unveiled two PCP refinement processes that operate postnatally, general narrowing of angle deviations and directed rotation. The postnatal narrowing of the orientation ranges from 33.2° in P2 to only 25.9° in adult WT OHC1s was completely impaired in *Cobl* KO mice (P2, 40.0°; adult OHC1s, 43.8°; Figure S6I versus Figure 5H).

Furthermore, orientations already successfully obtained by classical embryonic PCP signaling were not maintained in *Cobl* KO cochleae after birth. The orientation range of 42.4° for newborn *Cobl* KO OHC2s subsequently widened to 62.3° in adult OHC2s. OHC2 in adult *Cobl* KO cochleae thereby reached levels of misalignment almost as severe as those observed for OHC3s (67.7°) (Figure S6I versus Figure 5H).

Cobl-Dependent Postnatal PCP Refinements Are Executed during Cochlear Maturation Preceding Hearing Onset

Since PCP has to be actively maintained lifelong instead of being a robust tissue achievement provided by embryonic PCP signaling, we asked whether phenotypes seen in adult mice exclusively reflect maintenance defects during hearing or reflect impairments of postnatal refinements. We therefore conducted scanning EM analyses of P8 cochleae. At this stage, the auditory canal is still closed (Figures 6A and 6B) and the middle ear still filled with fluid. Interestingly, although not yet exposed to the physical stresses of sound, the ranges of stereocilia bundle deviations were already increased in the OHCs of *Cobl* KO pups (Figure 6C). Also, stereocilia bundle orientations in all three P8 OHC rows already showed a directed shift toward positive directions as in adult cochleae. The absolute differences were less

(C) Absolute values of deviations from 0° (irrespective of direction of misalignment).

(D–F) Angle distribution analyses of OHC3 (D), OHC2 (E), and OHC1 (F). Note the already widened deviation ranges and the directed rotational defects.

(G–I) Directional evaluations of orientation angle deviations of OHC1 (G), OHC2 (H), and OHC3 (I).

Data, mean and SEM. n = 1,172–1,354 hair cell bundles/row; 14–51 images/cochlea; WT/KO 5/3 animals and cochleae. **p < 0.01; ***p < 0.001. Two-way ANOVA/Bonferroni's (C) and D'Agostino normality test/Mann-Whitney U (D–I), respectively. See also Figure S6 for P2 data.

pronounced (about 2° each) than at later times. However, already at P8, they were statistically highly significant in all rows (Figures 6D–6I).

Cobl therefore plays an important role in postnatal PCP refinements that are part of a cochlear maturation program initiated prior to hearing onset.

Cobl KO Mice Show Hearing Impairments Reflecting Defects in the Cochlear Amplifier

Finally, we addressed whether the defects in the orientations of OHC stereocilia bundles may be associated with any defects in integrity and functionality of the cochlea. The OHC arrays of cochleae from WT and *Cobl* KO mice showed that *Cobl* KO cochleae were not marked by array distortions by insertions of extra OHCs. Also distortions by lacking OHCs (free positions in array, gaps) were not frequent (2%–4%) and mostly comparable to irregularities also occurring in WT cochlear arrays. Only in OHC row 3, an increased frequency of gaps (1.5% in WT versus 4% in KO) became statistically significant in *Cobl* KO mice (Figures S7A–S7D). Since these findings were correlated with OHC3 also showing the severest early misrotations (Figures S6F–S6I), the slightly increased gap frequency in row 3 may suggest that misorientations of the sensory apparatus are mechanically detrimental for hair cell integrity. The observed gaps indeed reflected a lack of the entire OHC at the respective array position (Figures S7E and S7F), as it, for example, also occurs during age-related hearing loss (Bowl and Dawson, 2015). A trend toward a loss of hair cells was also observed for IHCs, whereas insertions again were at WT levels (Figures S7G and S7H).

At P2, however, no hair cell gaps were observed (Figure S7I). The gaps observed in adult *Cobl* KO cochleae are thus unrelated to classical embryonic PCP signaling defects but represent low-frequency deletions from previously properly patterned arrays.

Whereas *Cobl* KO did not seem to have effects on the integrity of hair cells that go much beyond the slow hair cell loss that also occurs with age, distortions in the carefully aligned cochlear array are more likely to have direct physiological consequences for hearing. To address this, we first excluded that *Cobl* KO mice may suffer from general hearing loss. The general waveform of evoked responses in auditory brainstem response (ABR) measurements was unaffected (Figure 7A). Also the latencies and the amplitudes of the individual ABR waves were not significantly different between *Cobl* KO and WT littermates for click stimulation ranging from 10 to 80 dB (not shown). ABR thresholds to tone burst stimulation were only mildly elevated, especially for low-frequency stimuli, such as 4 kHz (Figure 7B). Thus, general sound detection was not strongly impaired but at low frequencies showed some defects.

We next analyzed cochlear amplification. In the healthy cochlea, electromotility of OHCs leads to enhanced basilar membrane vibrations, which are back-propagated through the middle ear and can be measured as otoacoustic emissions. Over the entire frequency range, the intensities of distortion product otoacoustic emissions (DPOAEs) from adult (12–14 weeks) *Cobl* KO mice consistently were significantly lower than those of WT mice (Figure 7C). Cobl may contribute to shaping the tonotopic spread of cochlear amplification, for which distorsion product otoacoustic emissions are a sensitive measure. Taken together,

the *Cobl* KO-mediated defects in cochlear arrays are accompanied by defective cochlear amplification. Together, our data unveil that Cobl is critical for in part previously unnoticed, postnatal PCP refinement processes and for correlated structural organizations beneath stereocilia, which are important for proper functioning of the cochlear amplifier during hearing (Figure 7D).

DISCUSSION

The organ of Corti is a highly organized array of sensory cells generated by different developmental cell polarity programs. Here, we report that KO of the actin nucleator Cobl leads to defects in postnatal PCP refinement and to impaired OHC amplifier function in hearing.

Analyses of *Cobl* KO mice unveiled the existence of a specialized, Cobl-dependent F-actin subset in OHCs. F-actin formation in OHCs was required for proper PCM organization. The specific Cobl function identified is in line with Cobl being an evolutionary young, vertebrate-specific actin nucleator. In addition, Cobl functions may be backed up by its distant relative Cobl-like (Izadi et al., 2018). In contrast to the specialized functions of Cobl beneath the sensory structures of OHCs, the general F-actin-rich cell cortex represents a very basic cell-biological structure and can be expected to depend on actin nucleators, which are evolutionarily much older and less specialized.

The identified Cobl-dependent substereociliar F-actin subset seemed to be distinct from the F-actin bundles in OHC stereocilia, which protrude into the cell cortex as rootlets conferring stereocilia stability and proper morphology (Tilney et al., 1980; Kitajiri et al., 2010; Vranceanu et al., 2012; Szarama et al., 2012). Stereociliar length is sensitive to changes in F-actin bundling and dynamics. Loss of F-actin-bundling proteins localized to the stereocilia core usually causes stereocilia degeneration. Interference with actin cytoskeletal components localized to the tips of stereocilia, such as the myosin XVa/whirlin/eps8 complex, reduces stereociliar length and diminishes the height differences between stereocilia rows (Manor et al., 2011; Ebrahim et al., 2016). Interferences with proteins at the stereociliar base, such as CLIC5 and ERM proteins, lead to stereocilia enlargement and fusion (Salles et al., 2014). Finally, deletion of β- and γ-actin severely shortened stereocilia and led to losses of individual stereocilia, respectively (Perrin et al., 2010; McGrath et al., 2017). At the physiological level, such defects are associated with fast progressive hearing loss or deafness at birth. Our analyses showed that *Cobl* KO did not lead to any of such more classical phenotypes. Instead, *Cobl* KO phenotypes affected the cuticular plate actin cytoskeleton and structures embedded in it (see Figure 7D for summary).

The identified, very specific role of Cobl in OHCs is in line with Cobl's relatively high abundance in inner ear OHCs and especially in the cuticular plate. The decrease of Cobl-dependent, substereociliar F-actin in the cuticular plate was accompanied with several hair cell phenotypes. *Cobl* KO led to an impaired organization of the PCM of OHCs. These impairments were observed both prior and during the critical postnatal period of structural and functional maturation of the cochlea prior to onset of hearing (P8). Importantly, they were F-actin formation dependent as demonstrated by latrunculin A-mediated inhibition of
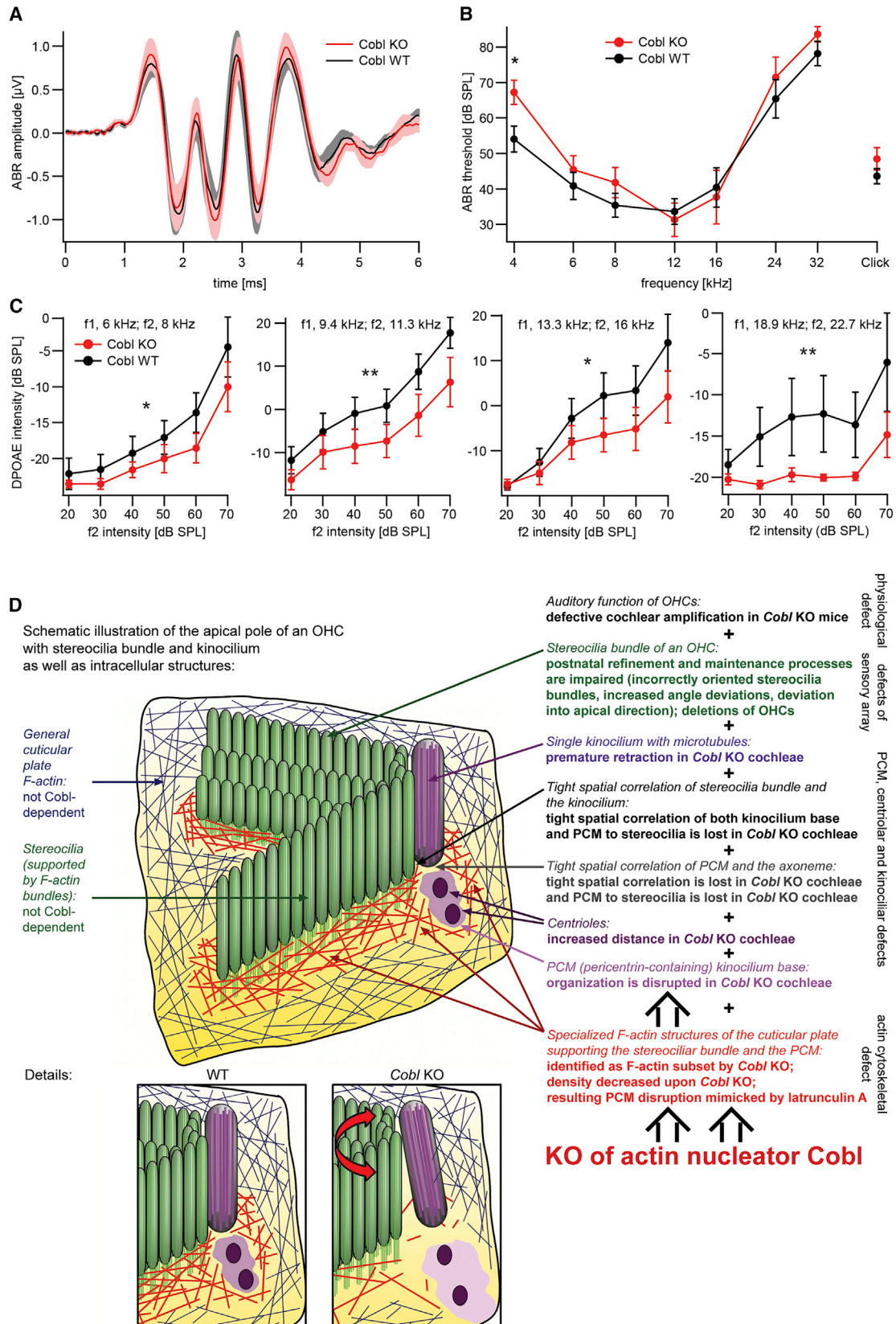
(legend on next page)

F-actin formation in WT cochleae. Interestingly, proper PCM organization furthermore turned out to be dependent on Ca^{2+}/calmodulin signaling. That both different inhibitors are phenocopying the PCM organization defects in *Cobl* KO is consistent with Cobl being (1) an actin nucleator (Ahuja et al., 2007) and (2) Ca^{2+}/calmodulin controlled (Hou et al., 2015).

These defects were accompanied by a loss of the spatial correlation of the centrioles, which are encased by the disorganized PCM. This *Cobl* KO phenotype may be in line with a suggested role of F-actin in centriole positioning (Tang and Marshall, 2012) and maybe also with recent reports describing some cross talk of centrosomes with the actin cytoskeleton—at least in less adherent cells, such as Jurkat, RPE1 cells and lymphocytes (Farina et al., 2016; Obino et al., 2016). We demonstrate the importance of the actin nucleator Cobl for the spatial organization of the PCM encasing the centriole-derived basal body of OHC kinocilia in the cochlea.

Mechanistically, it seems likely that Cobl-dependent, rather dynamic F-actin structures beneath the sensory apparatus help to encase and thereby spatially constrain the PCM. A rather static F-actin scaffold directly in the PCM to properly build the PCM or prevent the PCM from fragmentation seems unlikely because no F-actin can be observed in the PCM volume. It will therefore be interesting to evaluate whether Cobl has interaction partners in the PCM and/or at the basal body that may help to promote Cobl-mediated F-actin formation around the PCM. The PCM relations to cortical F-actin that we observed may furthermore relate to recent reports describing some sort of structural connections emanating from microtubular structures in the cuticular plate (Antonellis et al., 2014), some cross talk of the actin cytoskeleton with cilia during their embryonic migration (Ezan et al., 2013), RNAi against the PCM component PCM1 affecting the cloud-like F-actin mesh around related microtubule-based structures (centrosomes) in Jurkat cells, and the ability of isolated centrosomes to grow actin asters *in vitro* (Farina et al., 2016).

While the physiological relevance of the latter findings for centrosomes await further examinations, our data clearly show that Cobl-mediated disruption of cortical F-actin and of pericentriolar organization is linked to cell-biological processes that underlie the proper spatial arrangement of the sensory structures of OHCs. First, the distance of the disorganized PCM to the axoneme of the kinocilium was increased. Second, the distance of the PCM to the stereocilia bundle tip was increased. Accordingly, these defects coincided with an impaired spatial correlation of the normally intimately linked kinocilium base and the

stereocilia bundle in *Cobl* KO mice. It seems possible that the defects in basal body docking of the kinocilium with the stereocilia lead to the observed premature loss of kinocilia in *Cobl* KO mice during the critical time period prior to hearing onset (Figure 7D).

Cobl KO-mediated defects in kinocilium maintenance were observed at P8 and P9. This is in line with the observation that the *Cobl* KO defects in stereocilia bundle orientation also did not occur during classical embryonic PCP signaling, which is critical for PCP establishment and rough alignment of sensory cells prior to birth, but almost exclusively manifested postnatally. This provided an excellent possibility to specifically unveil thus far largely unknown postnatal planar polarity processes occurring subsequent to embryonic PCP establishment. In mutant mice lacking the functions of classical core PCP components, such as Frizzled or Celsr1, postnatal refinements are difficult to reveal because they are masked by the severe embryonal defects (Wang et al., 2006; Curtin et al., 2003). Comparisons of WT and *Cobl* KO cochleae from P2 and adult mice at ultra-high resolution clearly demonstrated that stereocilia bundle positioning angles are refined after birth to reach an even more aligned status in mature cochleae. An existence of postnatal refinement processes has already been suggested in earlier studies (Dabdoub et al., 2003; Copley et al., 2013). Our work shows that postnatal refinement narrowing the spread of orientation angles is completely disrupted upon *Cobl* KO.

Interestingly, all *Cobl* KO defects manifested before hearing onset, that is, between P2 and P8. During this time frame, hair cells are just probing transmission by self-activation (Johnson et al., 2013), but the hearing channel is still closed, the middle ear is still filled with fluid, and outside sounds cannot reach the inner ear. Thus, all forms of postnatal refinement we identified studying *Cobl* KO mice thus seem to be cochlea-autonomous processes independent of the physical pressures of sound.

Our analyses of *Cobl* KO mice furthermore revealed that the angle deviation status successfully reached by the embryonic PCP program has to be actively maintained after birth. The fact that both maintenance of embryonic PCP achievements and further postnatal refinements (angle fine-tuning and rotational refinement) are Cobl dependent strongly suggests that these processes are mechanistically related (Figure 7D).

The existence of postnatal planar polarity refinement and maintenance processes independent from classical embryonic PCP unraveled by *Cobl* KO is further supported by a previous observation of unknown, Vangl2-independent patterning mechanisms operating postnatally in cochleae from mice lacking the

Figure 7. *Cobl* KO Mice Show Hearing Impairments
(A) Averaged ABR waveforms evoked by 80-dB click stimulation in WT and *Cobl* KO mice (n = 11 WT and 11 KO mice; age, 12–14 weeks).
(B) ABR thresholds in *Cobl* KO mice compared to WT littermates.
(C) DPOAE intensities recorded from 11 WT and 11 KO mice in response to pairs of sine waves at different frequencies f1 and f2 unveiling an OHC amplifier defect. SPL, sound pressure level.
Data, mean ± SEM. (B) Mann-Whitney U: 4 kHz, *p = 0.0212; (C) two-way ANOVA across all intensities: 8 kHz, *p = 0.021; 11.3 kHz, **p = 0.001; 16 kHz, *p = 0.014; 22.7 kHz, **p = 0.001.
(D) Schematic illustrations of the apical pole of an OHC and of *Cobl* KO phenotypes. Red double-headed arrow (small panel) indicates the increased orientation variations observed for *Cobl* KO OHC stereociliar bundles. Black double arrows represent directly experimentally demonstrated causal relationships between (1) impairment of actin filament formation by LatA and PCM disorganization and (2) *Cobl* KO and each of the different phenotypes (numeration indicated by "+" signs).
See also Figure S7.

PCP core component Vangl2 (Montcouquiol et al., 2003; Copley et al., 2013). Parallel, somewhat related, but independent functions of Vangl2 and Cobl may finally also provide an explanation for *Vangl2*'s genetic interaction with the *Cobl*c101 gene trap mutation (Carroll et al., 2003).

The finding that misorientation of stereocilia bundles in *Cobl* KO worsened after hearing onset suggests that Cobl-mediated processes actively counteract the mechanical stress occurring during mechanotransduction and thereby prevent rotational shifts of the tip of the V-shaped bundle toward the apical turn of the cochlea. Thus, the achievements of embryonic PCP signaling have to be both refined and actively maintained after birth.

Two findings underscore the physiological importance of the postnatal processes executed by Cobl in the inner ear. First, OHC3, which showed the strongest defect in rotational refinement and premature kinocilium retraction during the critical time window of hearing onset, also showed the highest frequency in hair cell deletions in adult *Cobl* KO mice. Cobl-dependent postnatal refinements thus seem important for withstanding the mechanical stress during mechanotransduction after the onset of hearing and thereby ensure the integrity of the organ of Corti. It is therefore likely that defects in refinement and maintenance processes, such as those dependent on Cobl, are one of the cellular causes underlying the insidious loss of hair cells in age-related hearing loss.

Second, our analyses of otoacoustic emissions of *Cobl* KO mice showed that distortions of stereocilia bundle orientations caused by impaired, Cobl-dependent planar polarity refinement processes, which were linked to impaired PCM organization, were accompanied with disrupted alignment of the kinocilium with the stereociliar bundle, and with premature kinocilia retraction, and coincided with defects in the cochlear amplifier.

Thus, the ability to execute Cobl-dependent processes, which precisely fine-tune stereocilia bundle orientations postnatally to ensure a correct patterning of the inner ear sensory epithelium, is essential for cochlear amplification during hearing.

STAR★METHODS

Detailed methods are provided in the online version of this paper and include the following:

AUTHOR CONTRIBUTIONS

S.S., N.H., and C.A.H. generated *Cobl* KO mice. N.H. designed and conducted most of the experiments, analyzed data, and wrote the paper. S.N. was responsible for EM. N.S. designed and conducted audiophysiological measurements and analyzed the data. B.Q. and M.M.K. designed and supervised the study and wrote the paper.

DECLARATION OF INTERESTS

The authors declare no competing interests.

REFERENCES

Ahuja, R., Pinyol, R., Reichenbach, N., Custer, L., Klingensmith, J., Kessels, M.M., and Qualmann, B. (2007). Cordon-bleu is an actin nucleation factor and controls neuronal morphology. Cell *131*, 337–350.

Antonellis, P.J., Pollock, L.M., Chou, S.-W., Hassan, A., Geng, R., Chen, X., Fuchs, E., Alagramam, K.N., Auer, M., and McDermott, B.M., Jr. (2014). ACF7 is a hair-bundle antecedent, positioned to integrate cuticular plate actin and somatic tubulin. J. Neurosci. *34*, 305–312.

Bowl, M.R., and Dawson, S.J. (2015). The mouse as a model for age-related hearing loss—a mini-review. Gerontology *61*, 149–157.

Carroll, E.A., Gerrelli, D., Gasca, S., Berg, E., Beier, D.R., Copp, A.J., and Klingensmith, J. (2003). Cordon-bleu is a conserved gene involved in neural tube formation. Dev. Biol. *262*, 16–31.

Carvajal-Gonzalez, J.M., Roman, A.C., and Mlodzik, M. (2016). Positioning of centrioles is a conserved readout of Frizzled planar cell polarity signalling. Nat. Commun. *7*, 11135.

Copley, C.O., Duncan, J.S., Liu, C., Cheng, H., and Deans, M.R. (2013). Postnatal refinement of auditory hair cell planar polarity deficits occurs in the absence of Vangl2. J. Neurosci. *33*, 14001–14016.

Curtin, J.A., Quint, E., Tsipouri, V., Arkell, R.M., Cattanach, B., Copp, A.J., Henderson, D.J., Spurr, N., Stanier, P., Fisher, E.M., et al. (2003). Mutation of Celsr1 disrupts planar polarity of inner ear hair cells and causes severe neural tube defects in the mouse. Curr. Biol. *13*, 1129–1133.

Dabdoub, A., Donohue, M.J., Brennan, A., Wolf, V., Montcouquiol, M., Sassoon, D.A., Hseih, J.C., Rubin, J.S., Salinas, P.C., and Kelley, M.W. (2003). Wnt signaling mediates reorientation of outer hair cell stereociliary bundles in the mammalian cochlea. Development *130*, 2375–2384.

Doxsey, S.J., Stein, P., Evans, L., Calarco, P.D., and Kirschner, M. (1994). Pericentrin, a highly conserved centrosome protein involved in microtubule organization. Cell 76, 639–650.

Ebrahim, S., Ingham, N.J., Lewis, M.A., Rogers, M.J.C., Cui, R., Kachar, B., Pass, J.C., and Steel, K.P. (2016). Alternative splice forms influence functions of Whirlin in mechanosensory hair cell stereocilia. Cell Rep. 15, 935–943.

Ezan, J., and Montcouquiol, M. (2013). Revisiting planar cell polarity in the inner ear. Semin. Cell Dev. Biol. 24, 499–506.

Ezan, J., Lasvaux, L., Gezer, A., Novakovic, A., May-Simera, H., Belotti, E., Lhoumeau, A.C., Birnbaumer, L., Beer-Hammer, S., Borg, J.P., et al. (2013). Primary cilium migration depends on G-protein signalling control of subapical cytoskeleton. Nat. Cell Biol. 15, 1107–1115.

Farina, F., Gaillard, J., Guérin, C., Couté, Y., Sillibourne, J., Blanchoin, L., and Théry, M. (2016). The centrosome is an actin-organizing centre. Nat. Cell Biol. 18, 65–75.

Fettiplace, R., and Hackney, C.M. (2006). The sensory and motor roles of auditory hair cells. Nat. Rev. Neurosci. 7, 19–29.

Frolenkov, G.I., Belyantseva, I.A., Friedman, T.B., and Griffith, A.J. (2004). Genetic insights into the morphogenesis of inner ear hair cells. Nat. Rev. Genet. 5, 489–498.

Gasca, S., Hill, D.P., Klingensmith, J., and Rossant, J. (1995). Characterization of a gene trap insertion into a novel gene, cordon-bleu, expressed in axial structures of the gastrulating mouse embryo. Dev. Genet. 17, 141–154.

Gegg, M., Böttcher, A., Burtscher, I., Hasenoeder, S., Van Campenhout, C., Aichler, M., Walch, A., Grant, S.G., and Lickert, H. (2014). Flattop regulates basal body docking and positioning in mono- and multiciliated cells. eLife 3, e03842.

Haag, N., Schwintzer, L., Ahuja, R., Koch, N., Grimm, J., Heuer, H., Qualmann, B., and Kessels, M.M. (2012). The actin nucleator Cobl is crucial for Purkinje cell development and works in close conjunction with the F-actin binding protein Abp1. J. Neurosci. 32, 17842–17856.

Hou, W., Izadi, M., Nemitz, S., Haag, N., Kessels, M.M., and Qualmann, B. (2015). The actin nucleator Cobl is controlled by calcium and calmodulin. PLoS Biol. 13, e1002233.

Hou, W., Nemitz, S., Schopper, S., Nielsen, M.L., Kessels, M.M., and Qualmann, B. (2018). Arginine methylation by PRMT2 controls the functions of the actin nucleator Cobl. Dev. Cell 45, 262–275.e8.

Izadi, M., Schlobinski, D., Lahr, M., Schwintzer, L., Qualmann, B., and Kessels, M.M. (2018). Cobl-like promotes actin filament formation and dendritic branching using only a single WH2 domain. J. Cell Biol. 217, 211–230.

Jing, Z., Rutherford, M.A., Takago, H., Frank, T., Fejtova, A., Khimich, D., Moser, T., and Strenzke, N. (2013). Disruption of the presynaptic cytomatrix protein bassoon degrades ribbon anchorage, multiquantal release, and sound encoding at the hair cell afferent synapse. J. Neurosci. 33, 4456–4467.

Johnson, S.L., Kuhn, S., Franz, C., Ingham, N., Furness, D.N., Knipper, M., Steel, K.P., Adelman, J.P., Holley, M.C., and Marcotti, W. (2013). Presynaptic maturation in auditory hair cells requires a critical period of sensory-independent spiking activity. Proc. Natl. Acad. Sci. USA 110, 8720–8725.

Jones, C., Roper, V.C., Foucher, I., Qian, D., Banizs, B., Petit, C., Yoder, B.K., and Chen, P. (2008). Ciliary proteins link basal body polarization to planar cell polarity regulation. Nat. Genet. 40, 69–77.

Kelley, M.W., Driver, E.C., and Puligilla, C. (2009). Regulation of cell fate and patterning in the developing mammalian cochlea. Curr. Opin. Otolaryngol. Head Neck Surg. 17, 381–387.

Kitajiri, S., Sakamoto, T., Belyantseva, I.A., Goodyear, R.J., Stepanyan, R., Fujiwara, I., Bird, J.E., Riazuddin, S., Riazuddin, S., Ahmed, Z.M., et al. (2010). Actin-bundling protein TRIOBP forms resilient rootlets of hair cell stereocilia essential for hearing. Cell 141, 786–798.

Manor, U., Disanza, A., Grati, M., Andrade, L., Lin, H., Di Fiore, P.P., Scita, G., and Kachar, B. (2011). Regulation of stereocilia length by myosin XVa and whirlin depends on the actin-regulatory protein Eps8. Curr. Biol. 21, 167–172.

May-Simera, H.L., Petralia, R.S., Montcouquiol, M., Wang, Y.X., Szarama, K.B., Liu, Y., Lin, W., Deans, M.R., Pazour, G.J., and Kelley, M.W. (2015). Ciliary proteins Bbs8 and Ift20 promote planar cell polarity in the cochlea. Development 142, 555–566.

McGrath, J., Roy, P., and Perrin, B.J. (2017). Stereocilia morphogenesis and maintenance through regulation of actin stability. Semin. Cell Dev. Biol. 65, 88–95.

Montcouquiol, M., Rachel, R.A., Lanford, P.J., Copeland, N.G., Jenkins, N.A., and Kelley, M.W. (2003). Identification of Vangl2 and Scrb1 as planar polarity genes in mammals. Nature 423, 173–177.

Obino, D., Farina, F., Malbec, O., Sáez, P.J., Maurin, M., Gaillard, J., Dingli, F., Loew, D., Gautreau, A., Yuseff, M.I., et al. (2016). Actin nucleation at the centrosome controls lymphocyte polarity. Nat. Commun. 7, 10969.

Perrin, B.J., Sonnemann, K.J., and Ervasti, J.M. (2010). β-actin and γ-actin are each dispensable for auditory hair cell development but required for stereocilia maintenance. PLoS Genet. 6, e1001158.

Qualmann, B., and Kessels, M.M. (2009). New players in actin polymerization—WH2-domain-containing actin nucleators. Trends Cell Biol. 19, 276–285.

Ravanelli, A.M., and Klingensmith, J. (2011). The actin nucleator Cordon-bleu is required for development of motile cilia in zebrafish. Dev. Biol. 350, 101–111.

Salles, F.T., Andrade, L.R., Tanda, S., Grati, M., Plona, K.L., Gagnon, L.H., Johnson, K.R., Kachar, B., and Berryman, M.A. (2014). CLIC5 stabilizes membrane-actin filament linkages at the base of hair cell stereocilia in a molecular complex with radixin, taperin, and myosin VI. Cytoskeleton (Hoboken) 71, 61–78.

Schüler, S., Hauptmann, J., Perner, B., Kessels, M.M., Englert, C., and Qualmann, B. (2013). Ciliated sensory hair cell formation and function require the F-BAR protein syndapin I and the WH2 domain-based actin nucleator Cobl. J. Cell Sci. 126, 196–208.

Schwenk, F., Baron, U., and Rajewsky, K. (1995). A cre-transgenic mouse strain for the ubiquitous deletion of loxP-flanked gene segments including deletion in germ cells. Nucleic Acids Res. 23, 5080–5081.

Schwintzer, L., Koch, N., Ahuja, R., Grimm, J., Kessels, M.M., and Qualmann, B. (2011). The functions of the actin nucleator Cobl in cellular morphogenesis critically depend on syndapin I. EMBO J. 30, 3147–3159.

Sipe, C.W., and Lu, X. (2011). Kif3a regulates planar polarization of auditory hair cells through both ciliary and non-ciliary mechanisms. Development 138, 3441–3449.

Song, L., McGee, J., and Walsh, E.J. (2006). Frequency- and level-dependent changes in auditory brainstem responses (ABRS) in developing mice. J. Acoust. Soc. Am. 119, 2242–2257.

Szarama, K.B., Gavara, N., Petralia, R.S., Kelley, M.W., and Chadwick, R.S. (2012). Cytoskeletal changes in actin and microtubules underlie the developing surface mechanical properties of sensory and supporting cells in the mouse cochlea. Development 139, 2187–2197.

Tang, N., and Marshall, W.F. (2012). Centrosome positioning in vertebrate development. J. Cell Sci. 125, 4951–4961.

Tilney, L.G., Derosier, D.J., and Mulroy, M.J. (1980). The organization of actin filaments in the stereocilia of cochlear hair cells. J. Cell Biol. 86, 244–259.

Vranceanu, F., Perkins, G.A., Terada, M., Chidavaenzi, R.L., Ellisman, M.H., and Lysakowski, A. (2012). Striated organelle, a cytoskeletal structure positioned to modulate hair-cell transduction. Proc. Natl. Acad. Sci. USA 109, 4473–4478.

Wang, Y., Guo, N., and Nathans, J. (2006). The role of Frizzled3 and Frizzled6 in neural tube closure and in the planar polarity of inner-ear sensory hair cells. J. Neurosci. 26, 2147–2156.

STAR★METHODS

KEY RESOURCES TABLE

REAGENT or RESOURCE	SOURCE	IDENTIFIER
Antibodies		
Mouse monoclonal anti-acetylated tubulin	Sigma	RRID:AB_609894
Mouse monoclonal anti-Arl13b	Neuromab	RRID:AB_2341543
Guinea pig polyclonal anti-Cobl[DBY]	Haag et al., 2012	N/A
Guinea pig polyclonal anti-Cobl[ARA]	Schwintzer et al., 2011	N/A
Rabbit polyclonal anti-oncomodulin	Swant	RRID:AB_2313681
Rabbit polyclonal anti-Par6b (M-64)	Santa Cruz	RRID:AB_2267889
Guinea pig polyclonal anti-parvalbumin	Swant	RRID:AB_2665495
Rabbit polyclonal anti-pericentrin	Abcam	RRID:AB_304461
Rabbit polyclonal anti-aPKCζ (C-20)	Santa Cruz	RRID:AB_2300359
Rabbit polyclonal anti-β-tubulin	Synaptic Systems	RRID:AB_10637424
Mouse monoclonal anti-γ-tubulin (GTU-88)	Sigma	RRID:AB_477584
Alexa Fluor 488-labeled goat anti-guinea pig	Molecular Probes	RRID:AB_142018
Alexa Fluor 568-labeled goat anti-guinea pig	Molecular Probes	RRID:AB_141954
Alexa Fluor 488-labeled donkey anti-mouse	Molecular Probes	RRID:AB_141607
Alexa Fluor 568-labeled donkey anti-mouse	Molecular Probes	RRID:AB_2534013
Alexa Fluor 647-labeled goat anti-mouse	Molecular Probes	RRID:AB_141725
Alexa Fluor 488-labeled donkey anti-rabbit	Molecular Probes	RRID:AB_141708
Alexa Fluor 568-labeled goat anti-rabbit	Molecular Probes	RRID:AB_143011
Alexa Fluor 647-labeled goat anti-rabbit	Molecular Probes	RRID:AB_141775
Alexa Fluor 680-labeled goat-anti-rabbit	Molecular Probes	RRID:AB_2535758
Alexa Fluor 680-labeled goat-anti-mouse	Molecular Probes	RRID:AB_1965956
DyLight800-conjugated goat anti-rabbit	Thermo Fisher	RRID:AB_2556775
DyLight800-conjugated goat anti-mouse	Thermo Fisher	RRID:AB_2556774
IRDye680-conjugated donkey anti-guinea pig	LI-COR Bioscience	RRID:AB_10956079
IRDye800-conjugated donkey anti-guinea pig	LI-COR Bioscience	RRID:AB_1850024
Bacterial and Virus Strains		
E. coli commercial strain XL-10 Gold	Agilent	Cat#200314
E. coli commercial strain BL21-CodonPlus(DE3)-RIPL	Agilent	Cat#230280
Biological Samples		
Mouse (adult C57BL/6J) (different sorts of brain and cochlear material thereof)	Charles River	IMSR_JAX:000664
Chemicals, Peptides, and Recombinant Proteins		
α P^{32} dCTP, 100μCi, 3000Ci/mmol	Amersham	Cat#BLU013H100UC
AlexaFluor 488-conjugated phalloidin	Molecular Probes	Cat#A12379
AlexaFluor 647-conjugated phalloidin	Molecular Probes	Cat#A22287
DAPI	Molecular Probes	Cat#D1306
Latrunculin A	Tocris biosciences	Cat#3973
Calmodulin antagonist CGS9343B	Tocris biosciences	Cat#2255/10
Calmodulin antagonist W7 hydrochloride	Tocris biosciences	Cat#0369/100
Critical Commercial Assays		

REAGENT or RESOURCE	SOURCE	IDENTIFIER
NucleoSpin Plasmid	Macherey-Nagel	Cat#740.588.250
Rediprime II Random Prime Labeling System	GE Healthcare	Cat#RPN1633
RNase-free DNase kit	QIAGEN	Cat#79254
Deposited Data		
Original data	This paper	https://data.mendeley.com/datasets/ https://doi.org/10.17632/rypw3jv8mj.1
Experimental Models: Organisms/Strains		
Mouse strain C57BL/6J (WT and background for *Cobl* KO line)	Jackson Labs	IMSR_JAX:000664
Mouse strain *Cobl* KO C57BL/6J::129/SvJ (99,7::0,3 after speed congenics and backcrossing) (WT, KO and heterozygous littermates thereof)	This paper	N/A
Ubiquitously Cre recombinase expressing mice	Schwenk et al., 1995	N/A
Oligonucleotides		
Genotyping *Cobl* KO mice (WT; 388 bp): forward primer F1, 5′-acacagccctggcatcat-3′	This paper	N/A
Genotyping *Cobl* KO mice (WT; 388 bp): reverse primer R1, 5′-atacgggcaatcacgttttc-3′	This paper	N/A
Genotyping *Cobl* KO mice (KO; 235 bp): forward primer F1, 5′-acacagccctggcatcat-3′	This paper	N/A
Genotyping *Cobl* KO mice (KO; 235 bp): reverse primer R2, 5′-tgctccacactgaggtgttc-3′	This paper	N/A
RT-PCR Cobl: exon-spanning primer fwd-pan (E3/4) 5′-ggctcctgagaaatctgtacg-3′	This paper	N/A
RT-PCR Cobl: exon-spanning primer rev-pan (E4/5) 5′-ctaaacatttctcttctgttgtcc-3′	This paper	N/A
RT-PCR Cobl: exon-spanning primer fwd-WH2 (E12/13), 5′-gctccggaagactgcagaaca-3′	This paper	N/A
RT-PCR Cobl: exon-spanning primer rev-WH2 (E14/15), 5′-cgagcaagggaacctttcttagtc-3′	This paper	N/A
RT-PCR Cobl Δ10-15: fwd-Δ10-15 (E9), 5′-ccgagctccctaccctcctcctgacaca-3′	This paper	N/A
RT-PCR Cobl Δ10-15: rev-Δ10-15 (I9), 5′-tgggtaccgcaattcctggacaccaact-3′	This paper	N/A
RT-PCR GAPDH: exon-spanning primer forward, 5′-attgacctcaactacatggtctaca-3′	This paper	N/A
RT-PCR GAPDH: exon-spanning primer reverse, 5′-ccagtagactccacgacatactc-3′	This paper	N/A
Recombinant DNA		
129/SvJ mouse genomic λ library	Stratagene/Agilent	Cat#946313
pKO-DTA plasmid	Lexicon Genetics	N/A
Software and Algorithms		
AxioVision 4.8.2	Zeiss	SCR_002677
ZEN 2012	Zeiss	SCR_013672
Prism	GraphPad	SCR_002798
ImageJ	other	SCR_003070
Imaris	Bitplane	SCR_007370
BioSig32 operating software for TDT System II	Tucker-Davis Technologies	N/A
MaxQuant version 1.5.3.30	Max Planck Institute of Biochemistry	SCR_014485
BASReader 3.16 (FLA-3000 imager software)	Fuji	N/A

CONTACT FOR REAGENT AND RESOURCE SHARING

Further information and requests for resources and reagents should be directed to and will be fulfilled by the Lead Contact, Michael Kessels (Michael.Kessels@med.uni-jena.de).

EXPERIMENTAL MODEL AND SUBJECT DETAILS

E. coli Strain XL10 Gold

E. coli strain XL10 Gold (Stratagene/Agilent) (genomic information: endA1 glnV44 recA1 thi-1 gyrA96 relA1 lac Hte Δ(mcrA)183 Δ(mcrCB-hsdSMR-mrr)173 tet^R F'[proAB lacI^{q}ZΔM15 Tn10(Tet^R Amy Cm^R)]) was used for DNA plasmid amplifications. The strain was grown in LB-medium (Carl Roth GmbH & Co.KG) or on LB-agar (Carl Roth GmbH & Co.KG) with or without the respective antibiotics, which the strain carries resistances for (10 μg/ml tetracycline, 30 μg/ml chloramphenicol) or (if transformed) which the strain obtained resistances for by plasmid uptake (usually either 100 μg/ml ampicillin or 25 μg/ml kanamycin). The strain was usually either grown at 37°C or at RT.

E. coli Strain BL21-CodonPlus (DE3)-RIPL

E. coli strain BL21-CodonPlus (DE3)-RIPL (Stratagene/Agilent) (genomic information: *E. coli* B F– ompT hsdS(rB– mB–) dcm+ Tetr gal λ(DE3) endA Hte [argU proL Camr] [argU ileY leuW Strep/Specr]) was used for preparations of recombinant fusion proteins. The strain carries a resistance for tetracycline and was therefore either grown in LB-medium or on LB-agar with either tetracycline or other antibiotics (resistance acquired by transformation with suitable plasmid). The strain was either grown at 18°C, RT or 37°C.

Mice

Tissue material for RT-PCRs and Western blot analyses as well as brain sections and cochleae for immunohistochemistry were taken from WT (C57BL/6J) and *Cobl* KO mice of different developmental stages (see figure legends and Method Details).

Ubiquitously Cre recombinase expressing mice (Schwenk et al., 1995) were used for Cobl exon11 deletion.

Cobl KO mouse generation and backcrossings were done using C57BL/6J mice.

Cobl KO C57BL/6J::129/SvJ mice (99.7::0.3) were analyzed for cochlear defects.

METHOD DETAILS

Generation of *Cobl* KO Mice

The targeting vector was generated using a clone isolated from a 129/SvJ mouse genomic λ library (Agilent). An approximately 10 kb EcoRV fragment of this clone including exons 11–12 of the *Cobl* gene (GenBank: NC_000077.5, *Mus musculus*, chromosome 11) was cloned into the SmaI site of the pKO-DTA plasmid (Lexicon Genetics) with a phosphoglycerate kinase promoter-driven diphtheria toxin A cassette as a negative selection marker. A phosphoglycerate kinase promoter-driven neomycin resistance cassette (positive selection marker) flanked by frt sites and a loxP site was inserted into the AflII site of intron 10. A second loxP site together with an additional BamHI site was inserted into the SwaI site of intron 11. R1 mouse embryonic stem (ES) cells were electroporated with the NotI-linearized targeting vector. Genomic DNA of 288 Neomycin-resistant ES cell clones was screened by Southern blot with a P^{32}-labeled DNA probe (379 bp, nt 213457-213835, GenBank: NC_000077.5) after BamHI restriction (WT fragment: 9.3 kbp, nt 205809-215151; transgene fragment: 6.2 kbp, 208983-215151). One correctly targeted ES cell clone (B8) was injected into C57BL/6 blastocysts to generate chimeras. *Cobl* KO mice were obtained via mating with mice ubiquitously expressing Cre recombinase (Schwenk et al., 1995) to remove exon11 together with the selection cassette. Germline transmission successfully gave rise to a mouse line lacking the actin nucleator Cobl.

For genotyping, DNA of mouse tail biopsies was extracted with 10 mM Tris-HCl pH 8.0, 100 mM NaCl, 0.4 mg/ml proteinase K. After inactivation (10 min, 95°C), a high-speed supernatant was analyzed by PCR (fwd-primer F1 acacagccctggcatcat, rev-primers R1 (atacgggcaatcacgttttc) and R2 (tgctccacactgaggtgttc)). Primer combination F1/R1 amplified a 388 bp WT allele and primer combination F1/R2 a 235 bp KO allele.

The generation of *Cobl* KO mice and initial characterization was performed in strict compliance with the EU guidelines for animal experiments and was approved by the local government (permission number: 02-011/10; Thüringer Landesamt, Bad Langensalza; Germany).

Hearing physiological animal procedures were approved by the Niedersächsiches Landesamt für Verbraucherschutz und Lebensmittelsicherheit Oldenburg (permission number 33.9-42502-04-11/0415).

Experiments were done with both male and female mice 3-16 weeks (body weight) and with 12-14 weeks old male and female mice (hearing physiology), respectively.

Animals were kept in a C57BL/6J::129/SvJ (99,7::0,3) genetic background, bred heterozygously and housed under 14 h light/10 h dark conditions with *ad libitum* access to food and water.

Antibodies and Reagents

Primary antibodies were used according to Table S1. Affinity purifications of anti-Cobl antibodies were done and validated as described (Schwintzer et al., 2011; Haag et al., 2012). Secondary antibodies used included Alexa Fluor 488-, Alexa Fluor 568- and Alexa Fluor 647-conjugates (Molecular Probes) and antibodies coupled to IRDye680 and IRDye800 (LI-COR Biosciences), respectively.

Nuclei were visualized by co-staining with 0.1 mg/ml 4,6-diamidino-2-phenylindole (DAPI; Molecular Probes) and F-actin filaments using Alexa Fluor488- and Alexa Fluor647-conjugated phalloidin (Molecular Probes).

Latrunculin A (Tocris biosciences) was used at a concentration of 1 μM to inhibit actin polymerization.

To inhibit Ca^{2+}/calmodulin signaling, calmodulin antagonists W7 hydrochloride and CGS9343B (both Tocris biosciences) were used at a concentration of 10 μM in DMEM supplemented with 10% fetal calf serum (Thermo Fisher Scientific).

Reverse Transcription PCR (RT-PCR)

RNA isolation and RevT-PCR were performed as described (Haag et al., 2012). Briefly, tissue samples from cochleae and mouse brain were dissected, snap-frozen, and homogenized by grinding in liquid nitrogen and subsequently resuspended in Trizol reagent (Invitrogen). Two micrograms of DNase-treated (RNase-free DNase kit, QIAGEN) total RNA were reversely transcribed using oligo(dT)-primers and RevertAid H Minus Reverse Transcriptase (Fermentas). To test for the absence of contaminating genomic DNA, controls omitting the reverse transcriptase (- RevT) were run in parallel.

Cobl expression was analyzed by PCRs using the exon-spanning primers ggctcctgagaaatctgtacg (fwd-pan; exon 3/4), ctaaa catttctcttctgttgtcc (rev-pan; exon 4/5), gctccggaagactgcagaaca (fwd-WH2; exon 12/13), cgagcaagggaacctttcttagtc (rev-WH2; exon 14/15); ccgagctccctaccctcctcctgacaca (fwd-Δ10-15; exon 9); tgggtaccgcaattcctggacaccaact (rev-Δ10-15; intron 9) and GAPDH serving as control (fwd, attgacctcaactacatggtctaca; rev, ccagtagactccacgacatactc).

Zebrafish Whole-Mount In Situ Hybridization

Zebrafish whole mount *in situ* hybridizations were performed as described (Schüler et al., 2013). Sequences encoding for Cobl aa1-295 (sense and antisense) were used as probes. Images were recorded with a Zeiss Axio ZOOM.V16 microscope and analyzed with ZEN software (Zeiss).

Western Blot Analyses of Cochlea and Brain Lysates

Up to 10 cochleae from postnatal mice per genotype were dissected in protease inhibitor-containing 10 mM HEPES pH 7.4, pooled, collected and homogenized in lysis buffer (10 mM HEPES pH 7.4, 1 mM EGTA, 0.1 mM MgCl2, 1 mM EDTA, 1x protease inhibitor Complete) by sonication. Lysis was completed by addition of Triton X-100 (1% final) and incubation for 30 min at 4°C. After centrifugation (5000 × g, 10 min, 4°C), supernatants were precipitated with 4 volumes of 100% acetone at −20°C, washed with 80% acetone and resuspended in 2xSDS sample buffer (2% w/v SDS, 20% w/v glycerol, 10% β-mercaptoethanol, 125 mM Tris-HCl, pH 6.8, bromophenol blue).

Cochlea samples were analyzed by immunoblotting (70 μg protein/lane) with guinea pig anti-Cobl[DBY] antibodies, guinea pig anti-Cobl[ARA] antibodies (guinea pig anti-Cobl[ARA], no detection of Cobl in cochlea due to low abundance of Cobl and reduced sensitivity compared to guinea pig anti-Cobl[DBY] antibodies) and mouse anti-β-tubulin antibodies (loading control).

Mouse brain tissue was homogenized in ice-cold homogenization buffer (5 mM HEPES, pH 7.4, 320 mM sucrose, 1x protease inhibitor Complete) using a Potter S homogenizer (Sartorius) and centrifuged (1000 × g, 10 min at 4°C). The supernatant S1 was kept and combined with S1' obtained by a second round of reextraction of the pellet fraction P1 and centrifugation. The resulting supernatant (S1+S1') was centrifuged at 12000 × g (20 min at 4°C) and analyzed as supernatant (S2) and pellet (P2) fractions by anti-Cobl immunoblotting.

Inner Ear Immunohistochemistry, Confocal Imaging and Quantitative Morphometric Analysis

Animals were sacrificed, the temporal bones were removed, organs of Corti were dissected in PBS pH 7.4, and the Reissner's and tectorial membranes were carefully removed.

After fixation in 4% PFA in PBS (1 h, on ice) and washing with PBS, cochleae were blocked with 10%–15% normal goat serum in PBS containing 0.1% Triton X-100 (block solution) (1-2 h, RT). Primary antibody incubations (see Table S1 for details) were done overnight at 4°C with gentle agitation. After washing, secondary antibody incubations (in block solution, 1 h, RT) and washing, cochleae were mounted (Fluoromount G; SouthernBiotech) and confocal stacks were recorded from the apico-medial turn to ensure full developmental and morphological comparability (Leica TCS SP5; 63x/1.4 oil objective, LAS AF software). Image processing was done with ImageJ and/or Adobe Photoshop (without changing gamma adjustments).

Cuticular plate thicknesses in P8 cochleae were measured in X-Z-projections of the apical phalloidin staining. For this purpose, *Cobl* KO cochleae were stained together with WT OHCs in the same staining solution. Cuticular plate F-actin intensity and distributions were recorded at substereociliar positions (line scans 1) and at stereociliar-free positions (line scans 2) and analyzed in a blinded manner (n = 33 OHC3s for each genotype taken from 3 WT and 4 KO animals).

For kinocilium retraction analyses, confocal z stacks of anti-acetylated tubulin (kinocilium marker (Jones et al., 2008); confirmed by anti-Arl13b immunolabeling) immunolabeled apico-medial turns of whole-mount preparations of P2, P6, P8, P9 and P15 WT and *Cobl*

KO cochleae costained with anti-pericentrin antibodies (PCM marker) and phalloidin (stereocilia marker) were evaluated in a blinded manner. The evaluations of the presence or absence of anti-acetylated tubulin-stained kinocilium were done in 3D. n-numbers of OHCs evaluated: P2, 407 WT and 463 KO OHCs, 8 WT and 8 KO images, 4 WT and 4 KO animals. P6, 387 WT and 280 KO OHCs, 25 WT and 17 KO images, 2 animals each. P8, 692 WT and 769 KO OHCs, 20 WT and 22 KO images, 5 animals each. P9, 444 WT and 557 KO OHCs, 29 WT and 33 KO images, 2 animals each. P15, 120 WT and 175 KO OHCs, 11 WT and 17 KO images, 3 WT and 6 KO animals.

PCM analyses in WT and *Cobl* KO mice (P2, P8) were conducted by quantitative determinations of volume, sum intensity of anti-pericentrin labeling (i.e., integration of all fluorescence signals in the volume defined by 3D surface rendering) and density of anti-pericentrin labeling (average fluorescence signal per μm^3) in computed so-called 3D-surfaces (which represent the volume of the anti-pericentrin-marked PCM) that were obtained by surface rendering of confocal z stacks of the apico-medial turn of whole-mount preparations of P2 and P8 WT and *Cobl* KO cochleae costained with anti-acetylated tubulin antibodies (to correlate pericentrin PCM localization with the adjacent kinocilium) and with phalloidin (to mark the stereocilia bundle) using Imaris software (Bitplane) (absolute intensity, smooth 0.1). The n-numbers of kinociliar base structures evaluated were as follows: P2, 367 WT and 391 KO OHCs, 7 WT and 7 KO images, 4 WT and 4 KO animals. P8, 692 WT and 769 KO OHCs, 20 WT and 22 KO images, 5 animals each.

For further mechanistic analyses, P8 WT cochleae were incubated with the CaM inhibitors W7 (10 μM, 2 h, 0.1% DMSO final), CGS9343B (CGS, 10 μM, 2 h, RT, 0.1% DMSO final) and latrunculin A (LatA) (1 μM, 30 min, RT, 0.02% DMSO final), respectively, in DMEM/10% FCS (37°C, 5% CO2) prior to fixation. Evaluated were n = 63 OHCs (0.1%-DMSO-treated), 44 OHCs (W7) and 269 OHCs (CGS) from 3 P8 WT animals/cochleae per CaM inhibitor condition. In the LatA-treatments, n = 191 OHCs (DMSO) and 223 OHCs (LatA) from 4 P8 WT animals/cochleae per condition were evaluated.

Intercentriolar distances were analyzed in confocal z stacks of anti-γ-tubulin, anti-pericentrin and phalloidin-stained P2 cochleae subjected to anti-γ-tubulin surface rendering. The n-numbers of OHCs evaluated were: WT OHC3, 31; KO OHC3, 50; WT OHC2, 21; KO OHC2, 27; WT OHC1, 9; KO OHC1, 20 from 3 animals/cochleae each. The analyses were conducted by independent researchers in a fully blinded manner.

Measurements of the distance between the apical pole of the pericentrin-marked PCM and the base of the kinocilium (PCM-KC base distance) were also done in 3D surface renderings based on stacks of confocal images from mouse cochlear whole-mounts using IMARIS software. Cochleae were costained with phalloidin to visualize the stereocilia bundle and with anti-acetylated tubulin antibodies marking the kinocilium. Control experiments (coimmunolabelings) showed that anti-acetylated tubulin antibodies marked the kinocilium of OHCs similar to antibodies directed against the ciliary marker Arl13b. The n-numbers of PCM-KC base distance determinations were: 56-75 OHCs/row; total, 175 WT OHCs, 219 KO OHCs from 4 animals/genotype.

The distance from the PCM to the base of the stereocilia (SC) bundle tip was determined in 3D surface renderings of anti-pericentrin and phalloidin-stained cochlear whole-mounts (surface to surface measurements, as above, using IMARIS software). The n-numbers were: 49-75 OHCs/row; total, 171 WT OHCs, 224 KO OHCs; 4 animals/genotype.

The PCM distance from the symmetry axis of the stereocilia bundle was evaluated using the same 3D surface renderings. Top views were imaged and two perpendicular lines were drawn to mark the base of the V-shaped bundle and the perpendicular symmetry axis going through the tip of the stereocilia bundle. Distances between PCM (surface) and symmetry axis were determined in ° (in absolute values; using ImageJ). The n-numbers were: 221 WT OHCs, 234 KO OHCs from 4 animals/each genotype.

For frequency analyses of different phenotypes, the proportion of KO OHCs with data above the WT mean was plotted.

For neural tube and floor plate immunostainings, E9.5 WT and KO embryos were fixed with PFA (4% in PBS pH 7.4, 2 h at 4°C), cryoprotected (10% and 30% sucrose, o/n, 4°C), embedded in Tissue-Tek O.C.T. Compound (Sakura Finetek), cut transversely (section thickness, 16 μm) and subjected to immunohistochemistry as described (Haag et al., 2012).

Scanning EM and Quantitative Analyses of Hair Bundle Morphology

Dissected cochleae were immediately perfused with PBS and with pre-warmed fixative (2.5% glutaraldehyde in 0.1 M sodium cacodylate buffer pH 7.4). Cochleae were then immersion-fixed in the same fixative at RT (2 h) and at 4°C (o/n). Subsequently, the cochlear blocks were washed, dehydrated (ethanol series), critical point dried with liquid CO2 (CPD300, Leica), mounted on sample holders and post-dissected (removal of the bony shell as well as Reissner's and tectorial membranes) to expose the organ of Corti.

The specimen were sputtered with gold (SCD005 BAL-TEC) and examined with a field emission scanning EM (LEO1530, Zeiss; operated at 10 keV). All quantitative analyses were conducted in a fully blinded manner.

The number of inserted and deleted IHCs and OHCs were determined per 1000. Adult animals (12-15 weeks): WT, n = 7 animals/cochleae; KO n = 6 animals/cochleae (each with 17-53 pictures/cochlea and 101-356 IHCs/animal, 352-1129 OHCs/animal). P2 animals: n = 4 animals/cochleae per genotype (each with 11-57 pictures/cochlea and 20-250 IHCs/animal, 320-1651 OHCs/animal).

Scanning EM fine structure analyses of adult stereocilia bundles comprised assessments of the number of stereocilia per outer row (i.e., the tallest row) of the V-shaped bundle, row organization (number of stereocilia rows; supposed to be invariantly 3), missing stereocilia (visible as gaps), packing densities and positioning patterns (stacking) of stereocilia within the bundles, stereociliar heights (in tilts of the samples in the scanning EM; heights evaluated i) in absolute values (longest row) and ii) relative from row to row (gradation)). n = 32 WT and 31 KO OHC stereocilia bundles were evaluated. Measurements of length were done in n = 301 (WT) and n = 246 (KO) tallest-row stereocilia (from 4 WT and 4 KO mice and 2-10 stereocilia bundles/animal).

To measure OHC bundle orientation, the two ends of each individual V-shaped cilia bundle were connected and the deviation of this line from the 0° axis defined by the cell borders of row 1 OHCs and the Inner Pillar cells (0° axis, see scheme in Figure 5C) was determined.

Averaged stereocilia bundle orientations (bundle deviations from 0°C) were calculated by using the modulus of the orientation angles, i.e., irrespective of direction. This literature procedure was complemented by additional analyses, in which the direction of deviation was considered, too.

The distributions of stereocilia bundle orientations in adult WT and *Cobl* KO cochleae were plotted as percentage of hair cell bundles in a given deviation angle class with steps of 5° (considering the direction of deviation from 0°C).

Quantitative determinations of the ranges of stereocilia orientation angles were calculated considering 98% of the angles closest to mean.

For all the above detailed stereociliar orientation analyses, the n-numbers for adult mice (12-15 weeks) were n = 4 animals/cochleae each genotype, 17-53 pictures/cochlea, 141-916 OHCs/animal and 705-874 hair cell bundles/row. For P8 pups, the n-numbers were n = 5 WT/3 KO P8 animals/cochleae, 14-51 images/cochleae, 302-1246 OHCs/animal and 1172-1354 hair cell bundles/row. For P2 pups, the n-numbers were n = 4 animals/cochleae each genotype, 11-57 pictures/cochleae, 111-413 OHCs/animal and 382-437 hair cell bundles/row.

The spatial correlation of the kinocilium position in relation to the stereocilia bundle of was addressed for P2 OHCs by measuring the distances between the bases of the kinocilium and the first side stereocilium of the V-shaped structure in top views of cochlear arrays. Although this type of measurement may grossly under-evaluate increases in the distance between kinocilium and the central tip stereocilia of the bundle (the V-shaped bundles usually show indented tips, i.e., do not exhibit a pointed V shape) – e.g., a doubling of the distance may only lead to about 30% in the measurements of the neighboring side of the triangle formed between central "tip" stereocilium, kinocilium and the first side stereocilium when tips are broad – these measurements were most useful, as the distance between first side stereocilium and kinocilium could always reliably be addressed, whereas sight on the base of the central tip stereocilium is often blocked due to the tip indention of the stereocilia bundle. Analyzed were n = 60 OHCs/row from 4 animals/cochleae each genotype.

Recordings of Auditory Brainstem Response and DPOAE

The physiological examinations of hearing thresholds and cochlear amplification were essentially done as described before (Jing et al., 2013). In brief, 12-14 weeks old animals (male and female) were anesthetized intraperitoneally with a combination of ketamine (125 mg/kg) and xylazine (2.5 mg/kg). The heart rate was monitored constantly and the core temperature was maintained constant at 37°C using a rectal temperature-controlled heating blanket (Hugo Sachs Elektronik; Harvard Apparatus).

For stimulus generation, presentation, and data acquisition a TDT System II (Tucker-Davis Technologies) run by BioSig32 software (TDT) was used. Sound pressure levels are provided in dB SPL RMS (tonal stimuli) or dB SPL peak equivalent (PE, clicks) and were calibrated using a 1/4″ microphone (Brüel & Kjaer). Tone bursts (12 kHz, 10 ms plateau, 1 ms cos2 rise/fall) or clicks of 0.03 ms were presented at 20 Hz or 100 Hz in the free field ipsilaterally using a JBL 2402 speaker (JBL & Co.).

The difference potential between vertex and mastoid subdermal needles was amplified (50,000 times), filtered (low pass: 4 kHz, high pass: 400 Hz) and sampled at a rate of 50 kHz for 20 ms, 2 × 2000 times to obtain two mean auditory brainstem responses (ABRs) for each sound intensity.

Hearing thresholds were determined with 10 dB precision as the lowest stimulus intensity that evoked a reproducible response waveform in both traces by visual inspection.

For DPOAEs, MF1 speakers (Tucker-Davis) were used to generate two primary tones (frequency ratio f2/f1: 1.2, intensity f2 = intensity f1 + 10 dB). Primary tones were coupled into the ear canal by a custom-made probe containing an MKE-2 microphone (Sennheiser) and adjusted to the desired sound intensities at the position of the ear drum as mimicked in a mouse ear coupler.

The microphone signal was amplified and digitalized (DMX 6 Fire; Terratec) and analyzed by fast Fourier transformation (MATLAB; MathWorks).

QUANTIFICATION AND STATISTICAL ANALYSIS

No statistical methods were used to predetermine sample size. All quantitative data shown represent mean and SEM. Statistical analyses were done using GraphPad Prism software using the tests specified in the figure legends. Comparisons of two conditions were tested by either D'Agostino normality test/Mann Whitney U or unpaired t test (normal data distribution). Multiple comparisons were tested by two-way-ANOVA with post-test (Tukey's, Sidak's, Bonferroni's). Connected datasets were analyzed using 1way ANOVA with post-test (Dunnett's, Dunn's).

Statistical significances were marked by * $p < 0.05$, ** $p < 0.01$ and *** $p < 0.001$ throughout.

DATA AND SOFTWARE AVAILABILITY

Original datasets are available at https://data.mendeley.com (https://doi.org/10.17632/rypw3jv8mj.1).